

# Northumbria Research Link

Citation: Yang, Liming, Shu, Chang, Chen, Zhen, Liu, Yangyang, Wang, Yan and Shen, Xiang (2021) High-order gas kinetic flux solver for simulation of two dimensional incompressible flows. *Physics of Fluids*, 33 (1). 017107. ISSN 1070-6631

Published by: American Institute of Physics

URL: <https://doi.org/10.1063/5.0032488> <<https://doi.org/10.1063/5.0032488>>

This version was downloaded from Northumbria Research Link:  
<http://nrl.northumbria.ac.uk/id/eprint/45269/>

Northumbria University has developed Northumbria Research Link (NRL) to enable users to access the University's research output. Copyright © and moral rights for items on NRL are retained by the individual author(s) and/or other copyright owners. Single copies of full items can be reproduced, displayed or performed, and given to third parties in any format or medium for personal research or study, educational, or not-for-profit purposes without prior permission or charge, provided the authors, title and full bibliographic details are given, as well as a hyperlink and/or URL to the original metadata page. The content must not be changed in any way. Full items must not be sold commercially in any format or medium without formal permission of the copyright holder. The full policy is available online: <http://nrl.northumbria.ac.uk/policies.html>

This document may differ from the final, published version of the research and has been made available online in accordance with publisher policies. To read and/or cite from the published version of the research, please visit the publisher's website (a subscription may be required.)



**Northumbria  
University**  
NEWCASTLE









**UniversityLibrary**

# High-order gas kinetic flux solver for simulation of two dimensional incompressible flows

Cite as: Phys. Fluids **33**, 017107 (2021); <https://doi.org/10.1063/5.0032488>

Submitted: 08 October 2020 . Accepted: 16 December 2020 . Published Online: 08 January 2021

 L. M. Yang (杨鲤铭),  C. Shu (舒昌),  Z. Chen (陈臻),  Y. Y. Liu (刘阳阳),  Y. Wang (王岩), and  X. Shen (沈翔)



View Online



Export Citation



CrossMark

## ARTICLES YOU MAY BE INTERESTED IN

[Three-dimensional high-order least square-based finite difference-finite volume method on unstructured grids](#)

Physics of Fluids **32**, 123604 (2020); <https://doi.org/10.1063/5.0032089>

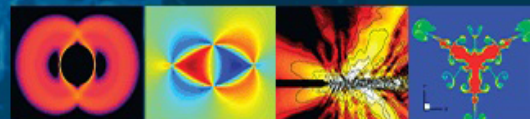
[Simulation of three-dimensional compressible decaying isotropic turbulence using a redesigned discrete unified gas kinetic scheme](#)

Physics of Fluids **32**, 125104 (2020); <https://doi.org/10.1063/5.0029424>

[A mass-conserved fractional step axisymmetric lattice Boltzmann flux solver for incompressible multiphase flows with large density ratio](#)

Physics of Fluids **32**, 103308 (2020); <https://doi.org/10.1063/5.0022050>

Physics of Fluids  
**GALLERY OF COVERS**



# High-order gas kinetic flux solver for simulation of two dimensional incompressible flows

Cite as: *Phys. Fluids* **33**, 017107 (2021); doi: [10.1063/5.0032488](https://doi.org/10.1063/5.0032488)

Submitted: 8 October 2020 • Accepted: 16 December 2020 •

Published Online: 8 January 2021









View Online



Export Citation



CrossMark

L. M. Yang (杨鲤铭),<sup>1,2</sup>  C. Shu (舒昌),<sup>2,a)</sup>  Z. Chen (陈臻),<sup>2</sup>  Y. Y. Liu (刘阳阳),<sup>2</sup>  Y. Wang (王岩),<sup>1</sup>   
and X. Shen (沈翔)<sup>3</sup> 

## AFFILIATIONS

<sup>1</sup>Department of Aerodynamics, College of Aerospace Engineering, Nanjing University of Aeronautics and Astronautics, Yudao Street, Nanjing, 210016 Jiangsu, China

<sup>2</sup>Department of Mechanical Engineering, National University of Singapore, 10 Kent Ridge Crescent, Singapore 119260

<sup>3</sup>Department of Mechanical and Construction Engineering, Northumbria University, Newcastle upon Tyne NE1 8ST, United Kingdom

<sup>a)</sup>Author to whom correspondence should be addressed: [mpeshuc@nus.edu.sg](mailto:mpeshuc@nus.edu.sg)

## ABSTRACT

Within the framework of the high-order finite volume (FV) method, a high-order gas kinetic flux solver (GKFS) is developed in this work for simulation of two-dimensional incompressible flows. Generally, in the conventional high-order FV method, the inviscid and viscous fluxes are treated separately. However, different from the conventional high-order FV method, the high-order GKFS evaluates the inviscid and viscous fluxes simultaneously from the local asymptotic solution to the Boltzmann equation, which consists of the equilibrium distribution function and its substantial derivative at the cell interface. By introducing a difference scheme with the high-order accuracy in space to discretize the substantial derivative, a high-order accurate local asymptotic solution to the Boltzmann equation can be obtained. The numerical flux of the Navier–Stokes equations can then be calculated by the moments of the local asymptotic solution. Since this local asymptotic solution is relatively simple, the numerical fluxes of the Navier–Stokes equations can be given explicitly for the high-order GKFS, which is the function of the left and the right states and their first-order derivatives. Numerical results showed that the developed solver can achieve the desired accuracy on both the quadrilateral mesh and the triangular mesh and its efficiency is higher than the second-order counterpart when achieving comparable accuracy of solution.

Published under license by AIP Publishing. <https://doi.org/10.1063/5.0032488>

## I. INTRODUCTION

Due to its high accuracy, the high-order method has been an important topic in the field of computational fluid dynamics (CFD). It has wide application in direct numerical simulation (DNS),<sup>1–4</sup> large eddy simulation (LES),<sup>5–8</sup> aeroacoustics,<sup>9–11</sup> etc. Nowadays, many high-order methods have been developed to address the challenging task of obtaining a high-order accurate, efficient, and robust solution of the Euler and Navier–Stokes equations. Some of the representative approaches include the high-order finite volume (FV),<sup>12–14</sup> the discontinuous Galerkin (DG),<sup>15–17</sup> the correction procedure using reconstruction (CPR),<sup>18,19</sup> the spectral volume (SV),<sup>20</sup> the spectral difference (SD),<sup>21</sup> and the weighted essential non-oscillatory (WENO)<sup>22–25</sup> methods. These methods have their advantages and disadvantages, and they provide different mathematical

frameworks to discretize the Euler and Navier–Stokes equations on structured or unstructured meshes.

Among the above-mentioned methods, the high-order FV scheme is relatively intuitive and convenient for application on unstructured meshes. In this method, the governing equation is discretized by the FV scheme and the functional value at the control volume is represented by a high-order approximation, such as the high-order Taylor series expansion,<sup>26</sup> the moving least-squares approximation,<sup>27</sup> the compact least-squares reconstruction,<sup>28</sup> and the radial basis function interpolation.<sup>29</sup> As a pioneering high-order FV scheme, the  $k$ -exact method approximates the functional value within each control volume by a modified Taylor series expansion,<sup>26,30,31</sup> which consists of the mean value and the spatial derivatives of the function. Similar to the second-order FV scheme, in the  $k$ -exact method, the mean value is updated directly by solving the

governing equation. To determine the spatial derivatives at the cell center, the modified Taylor series expansion needs to be integrated over the current cell and its neighboring cells. The resultant equation system connects the mean values of the current cell and its neighboring cells and the spatial derivatives at the center of the current cell. Correspondingly, the spatial derivatives can be obtained by solving the resulting equation system. Besides the  $k$ -exact method, a more straightforward high-order FV method, i.e., the least square-based finite difference-finite volume (LSFD-FV) method,<sup>32,33</sup> is developed recently. In this method, the functional value within each control volume is approximated by a conventional Taylor series expansion, which is based on the functional value and the spatial derivatives at the cell center. The functional value is obtained from the solution of the governing equation, and the spatial derivatives are calculated by the least square-based finite difference (LSFD) scheme from the functional values at the centers of the current cell and its neighboring cells. Due to its easy application, the LSFD-FV method is used in the present work to discretize the governing equation and approximate the functional value at each control volume.

Apart from the spatial discretization, in the high-order FV scheme, the calculation of numerical flux at the cell interface is another important issue. In conventional Navier–Stokes solvers,<sup>34–36</sup> the inviscid flux is usually calculated by the exact or approximate Riemann solver and the viscous flux is evaluated in a different way, which may cause degradation of accuracy or loss of consistency. Different from the conventional Navier–Stokes solvers, the gas kinetic scheme (GKS),<sup>37–40</sup> the gas kinetic flux solver (GKFS),<sup>41–44</sup> and the lattice Boltzmann flux solver (LBFS)<sup>45–48</sup> evaluate the inviscid and viscous fluxes simultaneously from the local solution to the Boltzmann equation at the cell interface. Specifically, the GKS calculates both the inviscid and viscous fluxes from the local integral solution to the Boltzmann equation at the cell interface and the GKFS and LBFS utilize the local asymptotic solution to the Boltzmann equation for this purpose. More recently, the second-order GKS has been extended to the high-order counterpart to improve accuracy.<sup>49–53</sup> In the high-order GKS, the numerical flux at the cell interface can achieve high-order accuracy in both space and time. However, since the coefficients related to the high-order derivatives are introduced into the local integral solution to the Boltzmann equation at the cell interface, the expression of numerical flux becomes very complicated and hard to be expressed explicitly. By applying the LBFS, the corresponding high-order FV scheme has also been developed by Liu *et al.*<sup>32,33</sup> In their work, the second-order LBFS is utilized directly to evaluate the numerical flux at the cell interface. Since the accuracy of the second-order LBFS is with regards to the streaming distance, which is usually smaller than the cell size, the overall accuracy of the high-order FV scheme may not be affected significantly. However, the streaming distance has to be chosen carefully to guarantee the overall accuracy.

In this work, we aim at extending the previous GKFS to the high-order one and implement it in the framework of the LSFD-FV method for simulation of incompressible flows. The local asymptotic solution to the Boltzmann equation used in GKFS consists of the equilibrium distribution function and its substantial derivative at the cell interface. In the previous GKFS,<sup>41,54</sup> the substantial derivative is discretized by a second-order difference scheme, resulting in a second-order flux solver in both space and time. To achieve the high-order accuracy, a difference scheme with the second-order

accuracy in time and the fourth-order accuracy in space is utilized to discretize the substantial derivative in this work. It is shown that the numerical flux of the Navier–Stokes equations can be given explicitly for the high-order GKFS, which is the function of the left and right states and their first-order derivatives. By applying the LSFD-FV method, these variables can be easily calculated by the high-order Taylor series expansion. In addition, to guarantee the temporal accuracy for simulation of unsteady problems, the multi-stage Runge–Kutta method<sup>55</sup> is adopted to discretize the governing equation in time. For steady problems, the implicit lower–upper symmetric Gauss–Seidel (LU-SGS) scheme<sup>56</sup> is utilized. To validate the developed high-order GKFS, a series of incompressible flow benchmark tests at various Reynolds numbers and/or with curved boundary are provided.

## II. NAVIER-STOKES EQUATIONS AND HIGH-ORDER FINITE VOLUME DISCRETIZATION

In this work, we confine the study to the isothermal incompressible flows, which are governed by the following weakly compressible Navier–Stokes equations under the low Mach number limit:

$$\frac{\partial \rho}{\partial t} + \nabla \cdot (\rho \mathbf{u}) = 0, \tag{1}$$

$$\frac{\partial \rho \mathbf{u}}{\partial t} + \nabla \cdot (\rho \mathbf{u} \mathbf{u} + p \mathbf{I}) = \nabla \cdot \left\{ \mu \left[ \nabla \mathbf{u} + (\nabla \mathbf{u})^T \right] \right\}, \tag{2}$$

where  $\rho$ ,  $\mathbf{u}$ ,  $p$ , and  $\mu$  are, respectively, the density, velocity, pressure, and dynamic viscosity. The pressure is calculated by  $p = \rho c_s^2$ , where  $c_s$  is the sound speed, which will be defined in Eq. (18).  $\mathbf{I}$  is the unit tensor. For the two-dimensional (2D) case, Eqs. (1) and (2) can be cast into a unified form as

$$\frac{\partial \mathbf{W}}{\partial t} + \nabla \cdot \mathbf{F} = \mathbf{0}. \tag{3}$$

Here, the conservative variable vector  $\mathbf{W}$  and the flux vector  $\mathbf{F}$  are given by

$$\mathbf{W} = \begin{bmatrix} \rho \\ \rho u \\ \rho v \end{bmatrix}, \mathbf{F} = \begin{bmatrix} F_\rho \\ F_{\rho u} \\ F_{\rho v} \end{bmatrix}. \tag{4}$$

Here,  $u$  and  $v$  are, respectively, the velocity components expressed in the  $x$ - and  $y$ -directions of the global Cartesian coordinate system.

To achieve the high-order accuracy, Eq. (3) is discretized by the cell-centered high-order FV scheme,

$$\frac{d}{dt} \left( \int_{\Omega_i} \mathbf{W} d\Omega \right) = - \sum_{j=1}^{N_f} \sum_{k=1}^{nGQp} (\mathbf{F}_k \cdot \mathbf{n}A)_j \omega_k, \tag{5}$$

where  $i$  is the index of the control volume,  $\Omega_i$  and  $N_f$  represent the volume and the number of faces of the control volume  $i$ , respectively,  $A$  denotes the area of the interface of the control volume,  $\mathbf{n} = (n_x, n_y)$  defines the unit normal vector of the cell interface in the global Cartesian coordinate system,  $nGQp$  is the number of Gaussian quadrature points on each cell interface, and  $\omega$  is the corresponding quadrature weight. For the fourth-order scheme used in this work,  $nGQp = 2$  is taken.

In the high-order LSFD-FV method,<sup>32,33</sup> the conservative variables are approximated by a Taylor series expansion at the cell center

with the designed order of accuracy. For the fourth-order scheme, the following third-order polynomial is adopted:

$$\begin{aligned} \mathbf{W}(x, y) = & \mathbf{W}_i + \frac{\partial \mathbf{W}}{\partial x} \Big|_i (x - x_i) + \frac{\partial \mathbf{W}}{\partial y} \Big|_i (y - y_i) \\ & + \frac{\partial^2 \mathbf{W}}{\partial x^2} \Big|_i \frac{(x - x_i)^2}{2} + \frac{\partial^2 \mathbf{W}}{\partial y^2} \Big|_i \frac{(y - y_i)^2}{2} \\ & + \frac{\partial^2 \mathbf{W}}{\partial x \partial y} \Big|_i (x - x_i)(y - y_i) + \frac{\partial^3 \mathbf{W}}{\partial x^3} \Big|_i \frac{(x - x_i)^3}{6} \\ & + \frac{\partial^3 \mathbf{W}}{\partial y^3} \Big|_i \frac{(y - y_i)^3}{6} + \frac{\partial^3 \mathbf{W}}{\partial x^2 \partial y} \Big|_i \frac{(x - x_i)^2 (y - y_i)}{2} \\ & + \frac{\partial^3 \mathbf{W}}{\partial y^2 \partial x} \Big|_i \frac{(y - y_i)^2 (x - x_i)}{2}. \end{aligned} \quad (6)$$

Here, the reference point  $(x_i, y_i)$  is the centroid of cell  $i$ . In Eq. (6), the derivatives are unknown. To determine the derivatives at control volume  $i$ , Eq. (6) is applied to the neighboring cells of cell  $i$ , which yields

$$\mathbf{S}_i d\mathbf{W}_i = \Delta \mathbf{W}_i, \quad (7)$$

where

$$\mathbf{S}_i = \begin{pmatrix} \Delta x_{i1} \Delta y_{i1} \frac{\Delta x_{i1}^2}{2} \frac{\Delta y_{i1}^2}{2} \Delta x_{i1} \Delta y_{i1} \frac{\Delta x_{i1}^3}{6} \frac{\Delta y_{i1}^3}{6} \frac{\Delta x_{i1}^2 \Delta y_{i1}}{2} \frac{\Delta y_{i1}^2 \Delta x_{i1}}{2} \\ \Delta x_{i2} \Delta y_{i2} \frac{\Delta x_{i2}^2}{2} \frac{\Delta y_{i2}^2}{2} \Delta x_{i2} \Delta y_{i2} \frac{\Delta x_{i2}^3}{6} \frac{\Delta y_{i2}^3}{6} \frac{\Delta x_{i2}^2 \Delta y_{i2}}{2} \frac{\Delta y_{i2}^2 \Delta x_{i2}}{2} \\ \vdots \quad \vdots \quad \vdots \quad \vdots \quad \vdots \quad \vdots \quad \vdots \quad \vdots \\ \Delta x_{iN} \Delta y_{iN} \frac{\Delta x_{iN}^2}{2} \frac{\Delta y_{iN}^2}{2} \Delta x_{iN} \Delta y_{iN} \frac{\Delta x_{iN}^3}{6} \frac{\Delta y_{iN}^3}{6} \frac{\Delta x_{iN}^2 \Delta y_{iN}}{2} \frac{\Delta y_{iN}^2 \Delta x_{iN}}{2} \end{pmatrix}, \quad (8)$$

$$d\mathbf{W}_i^T = \left[ \frac{\partial \mathbf{W}}{\partial x}, \frac{\partial \mathbf{W}}{\partial y}, \frac{\partial^2 \mathbf{W}}{\partial x^2}, \frac{\partial^2 \mathbf{W}}{\partial y^2}, \frac{\partial^2 \mathbf{W}}{\partial x \partial y}, \frac{\partial^3 \mathbf{W}}{\partial x^3}, \frac{\partial^3 \mathbf{W}}{\partial y^3}, \frac{\partial^3 \mathbf{W}}{\partial x^2 \partial y}, \frac{\partial^3 \mathbf{W}}{\partial y^2 \partial x} \right], \quad (9)$$

$$\Delta \mathbf{W}_i^T = [\mathbf{W}_{i1} - \mathbf{W}_i, \mathbf{W}_{i2} - \mathbf{W}_i, \dots, \mathbf{W}_{iN} - \mathbf{W}_i], \quad (10)$$

and  $\Delta x_{ij} = x_j - x_i$ ,  $\Delta y_{ij} = y_j - y_i$ ,  $j = 1, \dots, N$ , where  $N$  is the number of the neighboring cells of cell  $i$ . To avoid ill-conditioned and singular,  $N > 9$  is usually adopted and the local scaling technique and least square optimization are introduced to solve the equation system (7).<sup>57</sup> As a result,  $d\mathbf{W}_i$  can be approximated by the following matrix form:

$$d\mathbf{W}_i = \mathbf{K}_i \Delta \mathbf{W}_i, \quad (11)$$

where  $\mathbf{K}_i$  is a  $9 \times N$  dimensional weighting coefficient matrix, which is uniquely determined by the centroid of cell  $i$  and its neighboring cells.  $\mathbf{K}_i$  is calculated once and stored for the following computation to save the computational effort.

To update the conservative variables  $\mathbf{W}$  at the cell center, we need to substitute Eqs. (6) into (5), which yields

$$\frac{d}{dt} (\Omega_i \mathbf{W}_i + d\mathbf{W}_i^T \mathbf{C}_i) = \mathbf{R}_i, \quad (12)$$

with

$$\mathbf{C}_i^T = \left[ \overline{x^1 y^0}, \overline{x^0 y^1}, \frac{\overline{x^2 y^0}}{2}, \frac{\overline{x^0 y^2}}{2}, \overline{x^1 y^1}, \frac{\overline{x^3 y^0}}{6}, \frac{\overline{x^0 y^3}}{6}, \frac{\overline{x^2 y^1}}{2}, \frac{\overline{x^1 y^2}}{2} \right], \quad (13)$$

where  $\overline{x^n y^m}_i = \int_{\Omega_i} (x - x_i)^n (y - y_i)^m d\Omega$ .  $\mathbf{R}_i$  is residual and equals to the right-hand side of Eq. (5). Substituting Eqs. (11) into (12), we have

$$\frac{d}{dt} \left[ \left( \Omega_i - \sum_{k=1}^9 C_k^i \sum_{j=1}^N K_{kj}^i \right) \mathbf{W}_i + \sum_{j=1}^N \left( \sum_{k=1}^9 C_k^i K_{kj}^i \right) \mathbf{W}_{ij} \right] = \mathbf{R}_i. \quad (14)$$

For the problem with the fixed mesh, by applying Eq. (12) to all control volumes, the following matrix form can be obtained:

$$\mathbf{M} \frac{d\mathbf{W}}{dt} = \mathbf{R}. \quad (15)$$

Here,  $\mathbf{M}$  is a sparse coefficient matrix formed by coefficients on the left-hand side of Eq. (14). The conservative variables  $\mathbf{W}$  at the cell center can be updated by matching Eq. (15) in time. For unsteady problems, the explicit temporal discretization with point iterative method is used, and for steady problems, the implicit temporal discretization with LU-SGS method is adopted. The details can be found in Refs. 32 and 33.

### III. HIGH ORDER GAS KINETIC FLUX SOLVER

Apart from the spatial discretization, the evaluation of residual  $\mathbf{R}_i$  is another important issue in constructing the high-order scheme. As shown in Eq. (5), the key to calculate  $\mathbf{R}_i$  is to evaluate the numerical flux at the quadrature point of the cell interface. In this section, a high-order GKFS will be developed to play the role.

#### A. Boltzmann equation and its connection to Navier-Stokes equations

The GKFS uses the local asymptotic solution to the Boltzmann equation to calculate the flux of Navier-Stokes equations. In this process, the fundamental is the connection between the Boltzmann equation and the Navier-Stokes equations. For simulation of incompressible flows, the corresponding Boltzmann equation with the Bhatnagar-Gross-Krook (BGK) collision model is given by

$$\frac{\partial f}{\partial t} + \boldsymbol{\xi} \cdot \nabla f = \frac{g - f}{\tau}, \quad (16)$$

where  $f$  is the gas distribution function that varies with the physical space  $\mathbf{x}$ , the particle velocity space  $\boldsymbol{\xi}$ , and the time  $t$ .  $g$  is the equilibrium state given by

$$g = \rho \left( \frac{\lambda}{\pi} \right)^{\frac{D}{2}} e^{-\lambda \left[ \sum_{i=1}^D (\xi_i - u_i)^2 \right]}. \quad (17)$$

Here,  $u_i$  is the macroscopic flow velocity in the  $i$ th direction of  $D$ -dimensional space and  $\lambda = 1/(2RT)$ , where  $R$  and  $T$  are the gas constant and the temperature, respectively. For isothermal flows,  $RT$  is taken as the square of the sound speed, i.e.,  $RT = c_s^2 = u_0^2/Ma^2$ , where  $u_0$  is the reference velocity and  $Ma$  is the Mach number. In addition, the collision time scale  $\tau$  can be written as

$$\tau = \frac{\mu}{p} = \frac{\mu}{\rho c_s^2}. \quad (18)$$

Like the lattice Boltzmann method (LBM),<sup>58–60</sup> in this work, we choose the normalized sound speed as  $c_s = 1/\sqrt{3}$  and the normalized reference velocity as  $u_0 = 0.1$ .

According to the Chapman–Enskog expansion analysis,<sup>61</sup> the Navier–Stokes equations can be recovered by the Boltzmann equation with the first-order expansion to the distribution function in terms of the collision time scale,

$$f = g - \tau \left( \frac{\partial g}{\partial t} + \xi \cdot \nabla g \right) + O(\tau^2). \quad (19)$$

As a result, the numerical flux of the Navier–Stokes equations can be calculated by

$$\mathbf{F} = \langle \xi \boldsymbol{\varphi}_\alpha f \rangle, \quad (20)$$

where  $\langle \phi \rangle = \int_{-\infty}^{+\infty} \phi d\xi$  defines the integration of  $\phi$  over the particle velocity space.  $\boldsymbol{\varphi}_\alpha = (1, \xi)^T$  is the moment vector.

For ease of application on the unstructured mesh, a local coordinate system with  $x_1$ -axis pointing to the normal direction and  $x_2$ -axis aligning with the tangential direction of the cell interface is introduced. Supposing that the quadrature point of the cell interface is located at  $\mathbf{x} = \mathbf{0}$ , Eq. (19) can be rewritten as

$$f(\mathbf{0}, \xi, t) = g(\mathbf{0}, \xi, t) - \tau \left( \frac{\partial g}{\partial t} + \xi \cdot \nabla g \right) \Big|_{(\mathbf{0}, \xi, t)} + O(\tau^2). \quad (21)$$

Substituting Eqs. (21) into (20), the numerical flux of the Navier–Stokes equations at the quadrature point in the local coordinate system can be computed by

$$\bar{\mathbf{F}} = \langle \xi_1 \bar{\boldsymbol{\varphi}}_\alpha f \rangle, \quad (22)$$

where  $\bar{\boldsymbol{\varphi}}_\alpha = (1, \xi_1, \xi_2)^T$  is the moment vector and  $(\xi_1, \xi_2)$  are the components of the particle velocity expressed in the local coordinate system. Once  $\bar{\mathbf{F}}$  is obtained, the numerical flux in the global

Cartesian coordinate system can be calculated by

$$\mathbf{F} \cdot \mathbf{n} = \begin{bmatrix} 1 & 0 & 0 \\ 0 & n_x & -n_y \\ 0 & n_y & n_x \end{bmatrix} \bar{\mathbf{F}}. \quad (23)$$

It can be seen from Eq. (22) that, in GKFS, the key to calculate the numerical flux of the Navier–Stokes equations is to evaluate the distribution function at the cell interface.

## B. High-order approximation of distribution function at the cell interface

In the previous GKFS,<sup>32,33</sup> the second-order difference scheme is adopted to discretize the substantial derivative in Eq. (21). It only has the second-order accuracy in space and time. To construct the high-order GKFS, the distribution function  $f(\mathbf{0}, \xi, t)$  has to be approximated with high-order accuracy. In this work, the following fourth-order difference scheme is introduced:

$$\begin{aligned} f(\mathbf{0}, \xi, t^n + \Delta t_p) &= g(\mathbf{0}, \xi, t^n + \Delta t_p) + \frac{\tau}{6\Delta t_p} \left[ 2g(-3\xi\Delta t_p, \xi, t^n) \right. \\ &\quad - 9g(-2\xi\Delta t_p, \xi, t^n) + 18g(-\xi\Delta t_p, \xi, t^n) \\ &\quad \left. - 5g(\mathbf{0}, \xi, t^n) - 6g(\mathbf{0}, \xi, t^n + \Delta t_p) \right] \\ &\quad + O(\tau^2, \tau\Delta t_p, \tau|\xi|^4\Delta t_p^3), \end{aligned} \quad (24)$$

where  $\Delta t_p$  is the virtual time step size used in the solution reconstruction, which is determined by the following Courant–Friedrichs–Lewy (CFL) condition:<sup>62</sup>

$$\Delta t_p = \sigma_p \frac{\Omega}{(\Lambda_c^x + \Lambda_c^y) + C(\Lambda_v^x + \Lambda_v^y)}. \quad (25)$$

Here,  $\sigma_p$  is the associated CFL number,  $C = 4$  is a constant, and  $\Lambda_c$  and  $\Lambda_v$  are the convective spectral radii and the viscous spectral radii, respectively. In the solution reconstruction,  $\sigma_p$  should be less than one to satisfy the stability condition, which is different from the CFL number used for the calculation of the time step size for solving Eq. (15). Since  $|\xi|\Delta t_p$  is proportional to the mesh spacing  $h$ , if  $\Delta t_p > \tau$ , Eq. (24) has the second-order accuracy in time and the fourth-order accuracy in space.

In this work,  $t^n$  denotes the current time level whose flow variables are known. As a result, the equilibrium states that the surrounding points of the quadrature point can be approximated by the Taylor series expansion as follows:

$$\begin{aligned} g(-3\xi\Delta t_p, \xi, t^n) &= H(\xi_1)g_0^L \left[ 1 - 3a_1^L\xi_1\Delta t_p - 3a_2^L\xi_2\Delta t_p + \frac{9}{2}b_{11}^L(\xi_1\Delta t_p)^2 + \frac{9}{2}b_{22}^L(\xi_2\Delta t_p)^2 + 9b_{12}^L\xi_1\xi_2\Delta t_p^2 - \frac{9}{2}c_{111}^L(\xi_1\Delta t_p)^3 \right. \\ &\quad \left. - \frac{9}{2}c_{222}^L(\xi_2\Delta t_p)^3 - \frac{27}{2}c_{112}^L\xi_1^2\xi_2\Delta t_p^3 - \frac{27}{2}c_{122}^L\xi_1\xi_2^2\Delta t_p^3 \right] + (1 - H(\xi_1))g_0^R \left[ 1 - 3a_1^R\xi_1\Delta t_p - 3a_2^R\xi_2\Delta t_p \right. \\ &\quad \left. + \frac{9}{2}b_{11}^R(\xi_1\Delta t_p)^2 + \frac{9}{2}b_{22}^R(\xi_2\Delta t_p)^2 + 9b_{12}^R\xi_1\xi_2\Delta t_p^2 - \frac{9}{2}c_{111}^R(\xi_1\Delta t_p)^3 - \frac{9}{2}c_{222}^R(\xi_2\Delta t_p)^3 - \frac{27}{2}c_{112}^R\xi_1^2\xi_2\Delta t_p^3 - \frac{27}{2}c_{122}^R\xi_1\xi_2^2\Delta t_p^3 \right], \end{aligned} \quad (26)$$

$$\begin{aligned} g(-2\xi\Delta t_p, \xi, t^n) &= H(\xi_1)g_0^L \left[ 1 - 2a_1^L\xi_1\Delta t_p - 2a_2^L\xi_2\Delta t_p + 2b_{11}^L(\xi_1\Delta t_p)^2 + 2b_{22}^L(\xi_2\Delta t_p)^2 + 4b_{12}^L\xi_1\xi_2\Delta t_p^2 - \frac{4}{3}c_{111}^L(\xi_1\Delta t_p)^3 \right. \\ &\quad \left. - \frac{4}{3}c_{222}^L(\xi_2\Delta t_p)^3 - 4c_{112}^L\xi_1^2\xi_2\Delta t_p^3 - 4c_{122}^L\xi_1\xi_2^2\Delta t_p^3 \right] + (1 - H(\xi_1))g_0^R \left[ 1 - 2a_1^R\xi_1\Delta t_p - 2a_2^R\xi_2\Delta t_p + 2b_{11}^R(\xi_1\Delta t_p)^2 \right. \\ &\quad \left. + 2b_{22}^R(\xi_2\Delta t_p)^2 + 4b_{12}^R\xi_1\xi_2\Delta t_p^2 - \frac{4}{3}c_{111}^R(\xi_1\Delta t_p)^3 - \frac{4}{3}c_{222}^R(\xi_2\Delta t_p)^3 - 4c_{112}^R\xi_1^2\xi_2\Delta t_p^3 - 4c_{122}^R\xi_1\xi_2^2\Delta t_p^3 \right], \end{aligned} \quad (27)$$

$$\begin{aligned}
 g(-\xi\Delta t_p, \xi, t^n) = & H(\xi_1)g_0^L \left[ 1 - a_1^L \xi_1 \Delta t_p - a_2^L \xi_2 \Delta t_p + \frac{1}{2}b_{11}^L (\xi_1 \Delta t_p)^2 + \frac{1}{2}b_{22}^L (\xi_2 \Delta t_p)^2 + b_{12}^L \xi_1 \xi_2 \Delta t_p^2 - \frac{1}{6}c_{111}^L (\xi_1 \Delta t_p)^3 - \frac{1}{6}c_{222}^L (\xi_2 \Delta t_p)^3 \right. \\
 & \left. - \frac{1}{2}c_{112}^L \xi_1^2 \xi_2 \Delta t_p^3 - \frac{1}{2}c_{122}^L \xi_1 \xi_2^2 \Delta t_p^3 \right] + (1 - H(\xi_1))g_0^R \left[ 1 - a_1^R \xi_1 \Delta t_p - a_2^R \xi_2 \Delta t_p + \frac{1}{2}b_{11}^R (\xi_1 \Delta t_p)^2 + \frac{1}{2}b_{22}^R (\xi_2 \Delta t_p)^2 \right. \\
 & \left. + b_{12}^R \xi_1 \xi_2 \Delta t_p^2 - \frac{1}{6}c_{111}^R (\xi_1 \Delta t_p)^3 - \frac{1}{6}c_{222}^R (\xi_2 \Delta t_p)^3 - \frac{1}{2}c_{112}^R \xi_1^2 \xi_2 \Delta t_p^3 - \frac{1}{2}c_{122}^R \xi_1 \xi_2^2 \Delta t_p^3 \right], \tag{28}
 \end{aligned}$$

with the notations

$$\begin{aligned}
 g(\mathbf{0}, \xi, t^n) &= H(\xi_1)g_0^L + (1 - H(\xi_1))g_0^R, \\
 a_{10} &= \frac{\partial g_0}{\partial x_1}, \quad a_{20} = \frac{\partial g_0}{\partial x_2}, \quad b_{11}g_0 = \frac{\partial^2 g_0}{\partial x_1 \partial x_1}, \\
 b_{22}g_0 &= \frac{\partial^2 g_0}{\partial x_2 \partial x_2}, \quad b_{12}g_0 = \frac{\partial^2 g_0}{\partial x_1 \partial x_2}, \\
 c_{111}g_0 &= \frac{\partial^3 g_0}{\partial x_1 \partial x_1 \partial x_1}, \quad c_{222}g_0 = \frac{\partial^3 g_0}{\partial x_2 \partial x_2 \partial x_2}, \\
 c_{112}g_0 &= \frac{\partial^3 g_0}{\partial x_1 \partial x_1 \partial x_2}, \quad c_{122}g_0 = \frac{\partial^3 g_0}{\partial x_1 \partial x_2 \partial x_2}.
 \end{aligned}$$

The superscripts “L” and “R” denote, respectively, the variables at the left and right sides of the cell interface.  $H(\xi_1)$  is the Heaviside function, and  $H(\xi_1) = 1$  for  $\xi_1 \geq 0$  and  $H(\xi_1) = 0$  for  $\xi_1 < 0$ . Substituting Eqs. (26)–(28) into (24), we have

$$\begin{aligned}
 f(\mathbf{0}, \xi, t^n + \Delta t_p) &= g(\mathbf{0}, \xi, t^n + \Delta t_p) + \tau/\Delta t_p [g(\mathbf{0}, \xi, t^n) \\
 &\quad - g(\mathbf{0}, \xi, t^n + \Delta t_p)] - \tau [g_0^L (a_1^L \xi_1 + a_2^L \xi_2) H(\xi_1) \\
 &\quad + g_0^R (a_1^R \xi_1 + a_2^R \xi_2) (1 - H(\xi_1))]. \tag{29}
 \end{aligned}$$

As a result, the numerical flux of the Navier–Stokes equations can be calculated by substituting Eqs. (29) into (22), which yields

$$\begin{aligned}
 \bar{\mathbf{F}} &= (1 - \tau/\Delta t_p) \langle \xi_1 \bar{\boldsymbol{\varphi}}_\alpha g(\mathbf{0}, \xi, t^n + \Delta t_p) \rangle \\
 &\quad + \tau/\Delta t_p \langle H(\xi_1) \xi_1 \bar{\boldsymbol{\varphi}}_\alpha g_0^L [1 - \Delta t_p (a_1^L \xi_1 + a_2^L \xi_2)] \rangle \\
 &\quad + \tau/\Delta t_p \langle (1 - H(\xi_1)) \xi_1 \bar{\boldsymbol{\varphi}}_\alpha g_0^R [1 - \Delta t_p (a_1^R \xi_1 + a_2^R \xi_2)] \rangle. \tag{30}
 \end{aligned}$$

It can be seen that Eq. (30) only contains the first-order derivatives of the equilibrium distribution function at the left and right sides of the cell interface.

According to the definition of the expansion coefficients  $a_1$  and  $a_2$ , the following relationships can be obtained:

$$\langle a_1 \bar{\boldsymbol{\varphi}}_\alpha g_0 \rangle = (\partial \rho / \partial x_1, \partial \rho u_1 / \partial x_1, \partial \rho u_2 / \partial x_1)^T, \tag{31}$$

$$\langle a_2 \bar{\boldsymbol{\varphi}}_\alpha g_0 \rangle = (\partial \rho / \partial x_2, \partial \rho u_1 / \partial x_2, \partial \rho u_2 / \partial x_2)^T, \tag{32}$$

with

$$\begin{aligned}
 a_{10} &= a_{1,0} + a_{1,1} \xi_1 + a_{1,2} \xi_2, \\
 a_{20} &= a_{2,0} + a_{2,1} \xi_1 + a_{2,2} \xi_2.
 \end{aligned}$$

Here, the derivatives of conservative variables in the local coordinate system can be calculated from those in the global Cartesian coordinate system as follows:

$$\frac{\partial \rho u_1}{\partial x} = \frac{\partial \rho u}{\partial x} n_x + \frac{\partial \rho v}{\partial x} n_y, \quad \frac{\partial \rho u_1}{\partial y} = \frac{\partial \rho u}{\partial y} n_x + \frac{\partial \rho v}{\partial y} n_y, \tag{33}$$

$$\frac{\partial \rho u_2}{\partial x} = \frac{\partial \rho v}{\partial x} n_x - \frac{\partial \rho u}{\partial x} n_y, \quad \frac{\partial \rho u_2}{\partial y} = \frac{\partial \rho v}{\partial y} n_x - \frac{\partial \rho u}{\partial y} n_y, \tag{34}$$

$$\frac{\partial \psi}{\partial x_1} = \frac{\partial \psi}{\partial x} n_x + \frac{\partial \psi}{\partial y} n_y, \quad \frac{\partial \psi}{\partial x_2} = \frac{\partial \psi}{\partial y} n_x - \frac{\partial \psi}{\partial x} n_y. \tag{35}$$

In Eq. (35),  $\psi$  represents either  $\rho$ ,  $\rho u_1$ , or  $\rho u_2$ . Since the expansion coefficients  $a_1^L$ ,  $a_2^L$  and  $a_1^R$ ,  $a_2^R$  have similar expressions, in Eqs. (31) and (32), the superscripts “L” and “R” have been omitted for simplicity. As a result, for any expansion coefficient  $\phi$ , it can be computed by

$$\langle \phi \bar{\boldsymbol{\varphi}}_\alpha g_0 \rangle = (h_0, h_1, h_2)^T, \tag{36}$$

with

$$\phi = \phi_0 + \phi_1 \xi_1 + \phi_2 \xi_2, \tag{37}$$

where  $(h_0, h_1, h_2)^T$  is the right-hand side of Eqs. (31) or (32). Following the derivations given in Refs. 38 and 61, the expansion coefficient  $\phi$  can be expressed as

$$\phi_2 = 2\lambda (h_2 - u_2 h_0) / \rho, \tag{38}$$

$$\phi_1 = 2\lambda (h_1 - u_1 h_0) / \rho, \tag{39}$$

$$\phi_0 = h_0 / \rho - u_1 \phi_1 - u_2 \phi_2. \tag{40}$$

In addition, the equilibrium distribution functions  $g_0^L$  and  $g_0^R$  can be calculated from the conservative variables at the left and right sides of the cell interface, respectively. Applying Eq. (6) or the first-order derivatives of Eq. (6), both the conservative variables and their first-order derivatives at the left and right sides of the cell interface can be obtained by interpolation from the cell center.

The equilibrium distribution function at the cell interface  $g(\mathbf{0}, \xi, t^n + \Delta t_p)$  can be calculated by applying the compatibility condition to Eq. (29), which yields

$$\begin{aligned}
 \bar{\mathbf{W}} &= \langle H(\xi_1) \bar{\boldsymbol{\varphi}}_\alpha g_0^L [1 - \Delta t_p (a_1^L \xi_1 + a_2^L \xi_2)] \rangle \\
 &\quad + \langle (1 - H(\xi_1)) \bar{\boldsymbol{\varphi}}_\alpha g_0^R [1 - \Delta t_p (a_1^R \xi_1 + a_2^R \xi_2)] \rangle, \tag{41}
 \end{aligned}$$

where  $\bar{\mathbf{W}} = \langle \bar{\boldsymbol{\varphi}}_\alpha g(\mathbf{0}, \xi, t^n + \Delta t_p) \rangle$  is the conservative variable vector at the quadrature point of the cell interface at the time level  $t^n + \Delta t_p$ . Since  $g_0^L$ ,  $g_0^R$ ,  $a_1^L$ ,  $a_2^L$ ,  $a_1^R$ , and  $a_2^R$  have been determined previously,  $\bar{\mathbf{W}}$  can be obtained from Eq. (41) and  $g(\mathbf{0}, \xi, t^n + \Delta t_p)$  can be calculated by substituting  $\bar{\mathbf{W}}$  into Eq. (17).

### C. Conservative variables and numerical fluxes at the cell interface

In this section, the expressions of  $\bar{\mathbf{W}}$  and  $\bar{\mathbf{F}}$  will be given explicitly for the convenience of application. At first, some coefficients of the integral used in Eqs. (30) and (41) are introduced as follows:

$$\beta_0^L = \left[ \frac{1}{2} \operatorname{erfc}(-\sqrt{\lambda} u_1) \right]^L, \beta_1^L = u_1^L \beta_0^L + \left[ \frac{1}{2} \frac{e^{-\lambda u_1^2}}{\sqrt{\pi \lambda}} \right]^L,$$

$$\beta_2^L = u_1^L \beta_1^L + \frac{1}{2\lambda^L} \beta_0^L, \beta_3^L = u_1^L \beta_2^L + \frac{2}{2\lambda^L} \beta_1^L, \beta_4^L = u_1^L \beta_3^L + \frac{3}{2\lambda^L} \beta_2^L,$$

$$\beta_0^R = \left[ \frac{1}{2} \operatorname{erfc}(\sqrt{\lambda} u_1) \right]^R, \beta_1^R = u_1^R \beta_0^R - \left[ \frac{1}{2} \frac{e^{-\lambda u_1^2}}{\sqrt{\pi \lambda}} \right]^R,$$

$$\beta_2^R = u_1^R \beta_1^R + \frac{1}{2\lambda^R} \beta_0^R, \beta_3^R = u_1^R \beta_2^R + \frac{2}{2\lambda^R} \beta_1^R, \beta_4^R = u_1^R \beta_3^R + \frac{3}{2\lambda^R} \beta_2^R,$$

$$\gamma_1 = u_1, \gamma_2 = u_1^2 + \frac{1}{2\lambda}, \gamma_3 = u_1 \gamma_2 + \frac{2}{2\lambda} \gamma_1,$$

$$\chi_1 = u_2, \chi_2 = u_2^2 + \frac{1}{2\lambda}, \chi_3 = u_2 \chi_2 + \frac{2}{2\lambda} \chi_1.$$

Note that the expressions of coefficients without superscript can be used for both the left and right sides of the cell interface. As a result, the three components of  $\bar{\mathbf{W}}$  expressed in the local coordinate system can be written as

$$\bar{\mathbf{W}}(1) = \rho^L \beta_0^L + \rho^R \beta_0^R - \Delta t_p (\rho^L h_0^L + \rho^R h_0^R), \quad (42)$$

$$\bar{\mathbf{W}}(2) = \rho^L \beta_1^L + \rho^R \beta_1^R - \Delta t_p (\rho^L h_1^L + \rho^R h_1^R), \quad (43)$$

$$\bar{\mathbf{W}}(3) = \rho^L \beta_0^L \chi_1^L + \rho^R \beta_0^R \chi_1^R - \Delta t_p (\rho^L h_2^L + \rho^R h_2^R), \quad (44)$$

where

$$h_0 = a_{1,0} \beta_1 + a_{1,1} \beta_2 + a_{1,2} \beta_1 \chi_1 + a_{2,0} \beta_0 \chi_1 + a_{2,1} \beta_1 \chi_1 + a_{2,2} \beta_0 \chi_2,$$

$$h_1 = a_{1,0} \beta_2 + a_{1,1} \beta_3 + a_{1,2} \beta_2 \chi_1 + a_{2,0} \beta_1 \chi_1 + a_{2,1} \beta_2 \chi_1 + a_{2,2} \beta_1 \chi_2,$$

$$h_2 = a_{1,0} \beta_1 \chi_1 + a_{1,1} \beta_2 \chi_1 + a_{1,2} \beta_1 \chi_2 + a_{2,0} \beta_0 \chi_2 + a_{2,1} \beta_1 \chi_2 + a_{2,2} \beta_0 \chi_3.$$

Similarly, the three components of  $\bar{\mathbf{F}}$  can be computed by

$$\bar{\mathbf{F}}(1) = \rho u_1, \quad (45)$$

$$\bar{\mathbf{F}}(2) = (1 - \tau / \Delta t_p) \rho \gamma_2 + \tau / \Delta t_p (\rho^L \beta_2^L + \rho^R \beta_2^R) - \tau (\rho^L \chi_1^L + \rho^R \chi_1^R), \quad (46)$$

$$\bar{\mathbf{F}}(3) = (1 - \tau / \Delta t_p) \rho \gamma_1 \chi_1 + \tau / \Delta t_p (\rho^L \beta_1^L \chi_1^L + \rho^R \beta_1^R \chi_1^R) - \tau (\rho^L \chi_2^L + \rho^R \chi_2^R), \quad (47)$$

where

$$\lambda_1 = a_{1,0} \beta_3 + a_{1,1} \beta_4 + a_{1,2} \beta_3 \chi_1 + a_{2,0} \beta_2 \chi_1 + a_{2,1} \beta_3 \chi_1 + a_{2,2} \beta_2 \chi_2,$$

$$\lambda_2 = a_{1,0} \beta_2 \chi_1 + a_{1,1} \beta_3 \chi_1 + a_{1,2} \beta_2 \chi_2 + a_{2,0} \beta_1 \chi_2 + a_{2,1} \beta_2 \chi_2 + a_{2,2} \beta_1 \chi_3.$$

Note that, in Eqs. (45)–(47), the flow variables without superscripts “L” and “R” are determined from  $\bar{\mathbf{W}}$ . Comparatively, the expressions of the numerical flux of the Navier–Stokes equations given by the high-order GKFS are more concise than those of the high-order GKS.<sup>49–53</sup>

## IV. NUMERICAL EXAMPLES

In this section, the performance of the present high-order GKFS is validated by several test examples, including the decaying vortex flow, the lid-driven cavity flow, the polar cavity flow, the flow around a circular cylinder, and the flow around a NACA0012 airfoil. Unless otherwise stated, the implicit temporal discretization with LU-SGS method is used to solve Eq. (15). All the computations were carried out on a workstation with a processor of Intel(R) Xeon(R) E5-2687 CPU@3.0 GHz. For convenience, the second-order GKFS and the high-order GKFS are abbreviated as “2O GKFS” and “HO GKFS,” respectively.

### A. Case 1: Decaying vortex flow

The numerical accuracy of the developed solver is first examined by simulating the decaying vortex flow, which has analytical solutions as follows:

$$\begin{aligned} \rho(x, y, t) &= \rho_0 - \frac{\rho_0 u_0^2}{4c_s^2} [\cos(2\pi x/L) + \cos(2\pi y/L)] e^{-4\pi^2 u_0 t / (ReL)}, \\ u(x, y, t) &= -u_0 \cos(\pi x/L) \sin(\pi y/L) e^{-2\pi^2 u_0 t / (ReL)}, \\ v(x, y, t) &= u_0 \sin(\pi x/L) \cos(\pi y/L) e^{-2\pi^2 u_0 t / (ReL)}, \end{aligned} \quad (48)$$

where  $\rho_0$  and  $u_0$  are the reference density and velocity. The Reynolds number is set as  $Re = \rho_0 u_0 L / \mu = 100$  and the computational domain is taken as  $[-L, L] \times [-L, L]$ . Initially, the values of density and velocity in the computational domain are assigned by Eq. (48) at time  $t = 0$ . The periodic boundary condition is imposed on four boundaries. The relative error of  $u$ -velocity at time  $t = 0.2 L / u_0$  is measured by the  $L_2$  norm to validate the convergence order numerically. In the simulation, the three-stage Runge–Kutta method is used for the temporal discretization. The  $u$ -velocity contours and  $v$ -velocity contours calculated by the high-order GKFS with a mesh size of  $h = 1/20$  are shown in Fig. 1, where the periodic distribution of the flow field is observed.

First, the accuracy of GKFS on the regular quadrilateral mesh and the regular triangular mesh is tested. Four mesh sizes of  $h = 1/10, 1/20, 1/40,$  and  $1/80$  are considered. The virtual time step size used in the solution reconstruction is taken as  $\Delta t_p = 0.2h \sin(\theta)$ , where  $\theta$  is the minimum interior angle among the left and right side cells of the interface. This setting is the same as the high-order FV scheme of Liu *et al.*<sup>32</sup> and also satisfies the constraint of Eq. (25). It can be seen from Figs. 2 and 3 that the desired accuracy can be achieved by the high-order GKFS for both the quadrilateral mesh and the triangular mesh. At the same time, as compared with the second-order GKFS, the high-order GKFS has a smaller relative error. Second, the effect of the virtual time step size on the accuracy of the high-order GKFS is investigated on the quadrilateral mesh. The results of



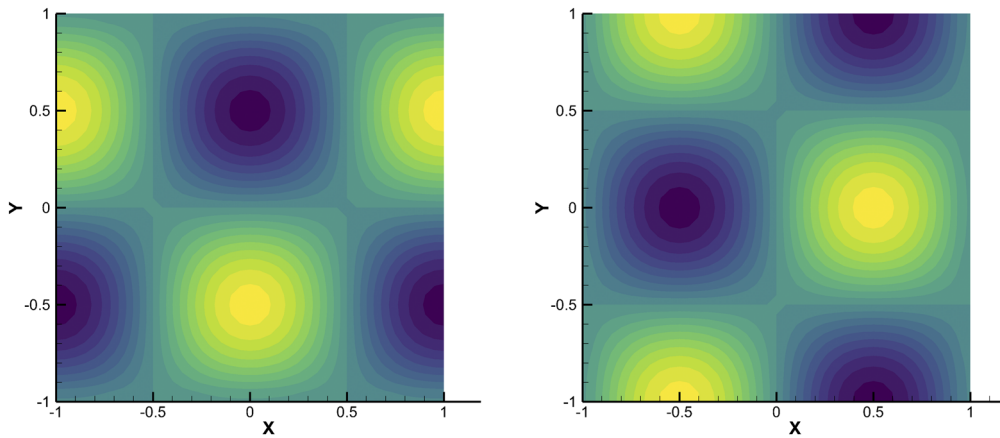


FIG. 1.  $u$ -velocity contours (left) and  $v$ -velocity contours (right) for decaying vortex flow calculated by the HO GKFS with a mesh size of  $h = 1/20$ .

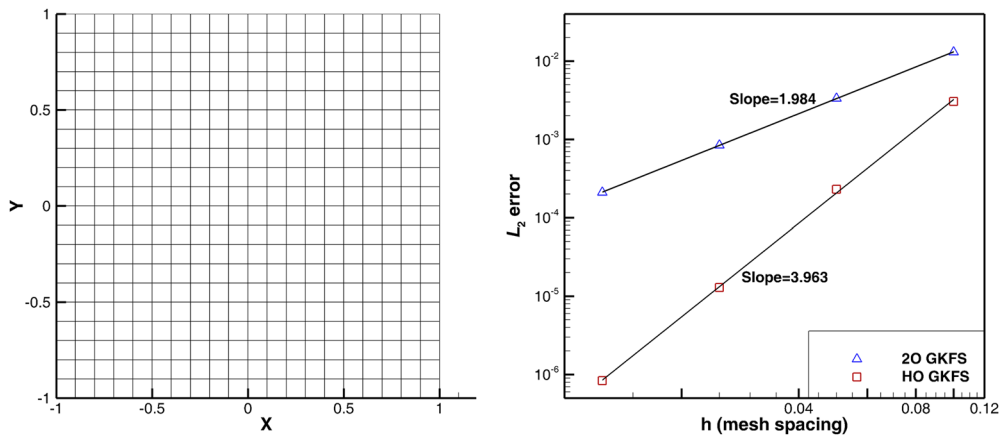


FIG. 2. Accuracy test for 2O GKFS and HO GKFS on the regular quadrilateral mesh.

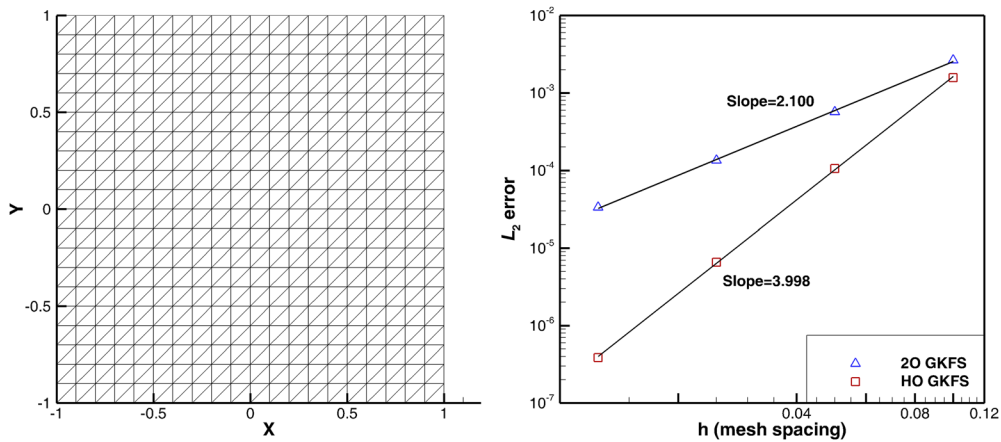


FIG. 3. Accuracy test for 2O GKFS and HO GKFS on the regular triangular mesh.

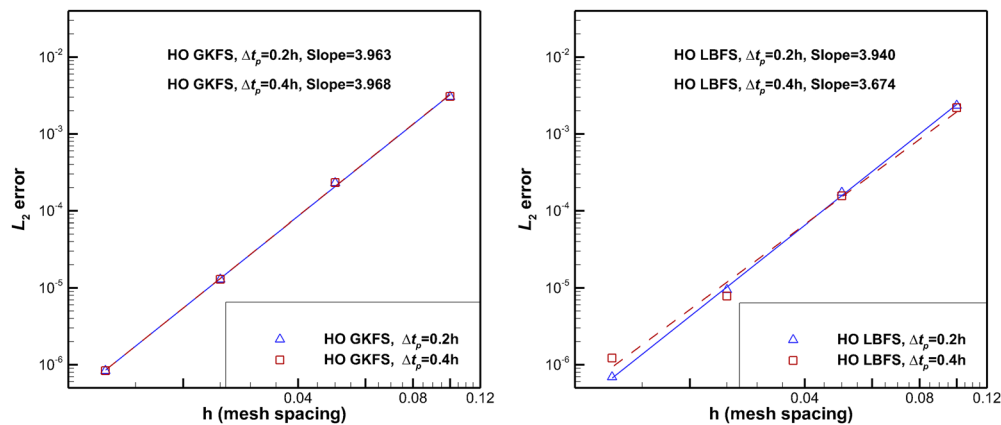


FIG. 4. Accuracy test for HO GKFS and HO LBFS with different virtual time step sizes of flux reconstruction.

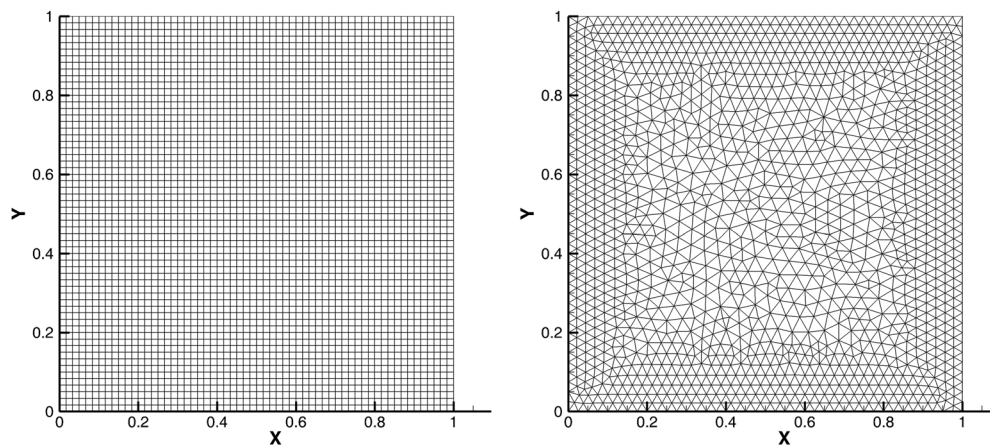


FIG. 5. Computational mesh for lid-driven cavity flow.

$\Delta t_p = 0.2h$  and  $\Delta t_p = 0.4h$ , which correspond to the CFL numbers of  $\sigma_p = 0.24$  and  $\sigma_p = 0.48$ , are compared in Fig. 4. Clearly, the accuracy of the high-order GKFS is not affected by the virtual time step size  $\Delta t_p$ . However, for the high-order FV scheme of Liu *et al.*,<sup>32</sup> which is labeled “HO LBFS,” the order of accuracy degrades as  $\Delta t_p$  is increased. The reason is that  $\Delta t_p = 0.4h$  will lead to the extrapolation for the HO LBFS, while the constraint of Eq. (25) is still satisfied for the HO GKFS.

**B. Case 2: Lid-driven cavity flow**

The second test case is the lid-driven cavity flow, which is used to compare the accuracy and efficiency of the high-order GKFS with the second-order one. The dynamic similarity of this test example depends on the Reynolds number, which is defined as  $Re = \rho_0 u_0 L / \mu$ , where  $\rho_0$  is the reference density,  $u_0$  is the velocity of the top lid, and  $L$  is the length of the square cavity. In the simulation, both the uniform quadrilateral mesh and the non-uniform triangular mesh shown in Fig. 5 are adopted, and the Reynolds number is taken as 1000. The streamlines of this test case are shown in Fig. 6,

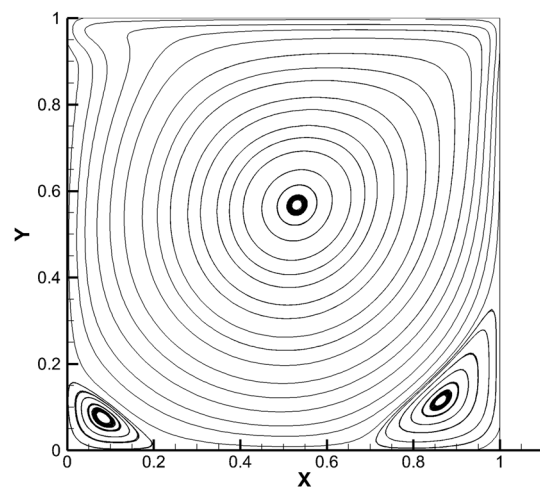


FIG. 6. Streamlines for lid-driven cavity flow calculated by the HO GKFS on a uniform quadrilateral mesh with 3600 cells.

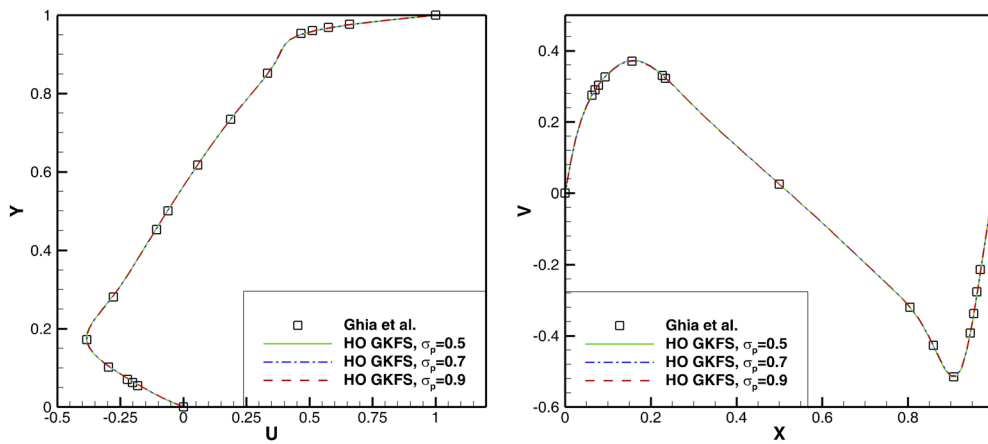


FIG. 7. Comparison of velocity profiles for lid-driven cavity flow obtained by the HO GKFS with different virtual time step sizes of flux reconstruction.

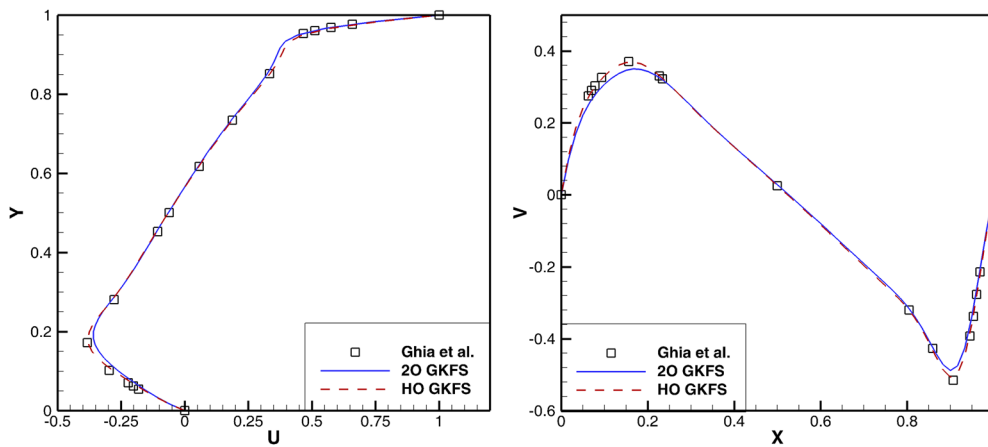


FIG. 8. Comparison of velocity profiles for lid-driven cavity flow obtained by the 20 GKFS and the HO GKFS on a uniform quadrilateral mesh with 3600 cells.

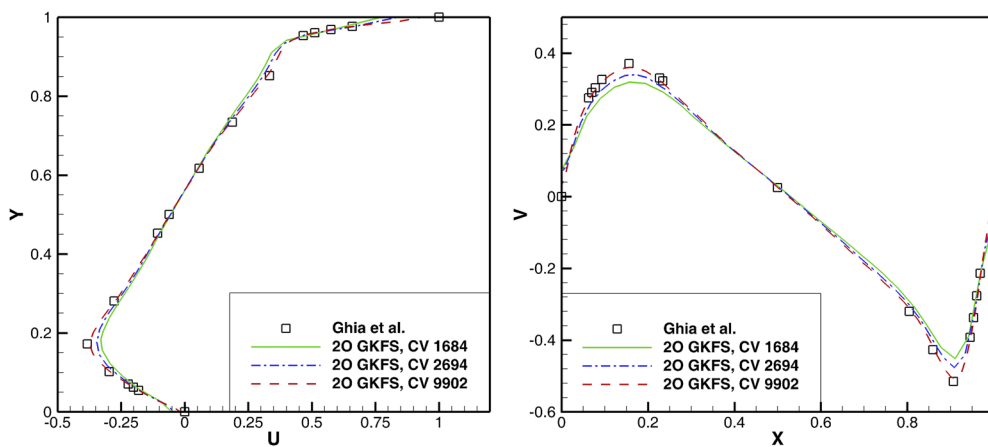


FIG. 9. Comparison of velocity profiles for lid-driven cavity flow obtained by the 20 GKFS on different triangular meshes. Note that "CV" means the number of control volumes, and this abbreviation is also used in the following figures.

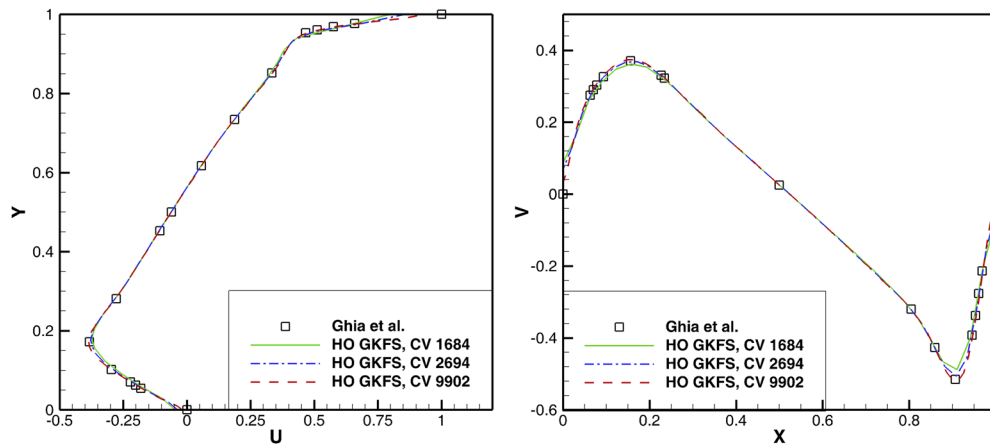


FIG. 10. Comparison of velocity profiles for lid-driven cavity flow obtained by the HO GKFS on different triangular meshes.

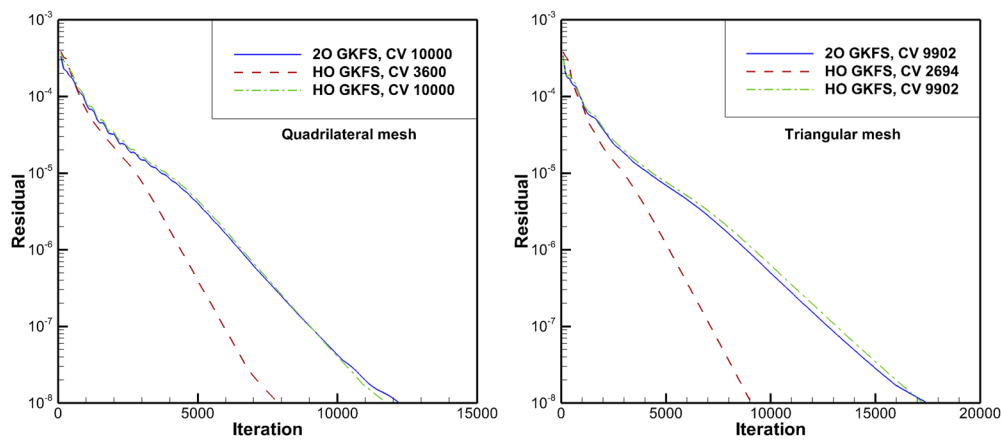


FIG. 11. Comparison of convergence histories of the 2O GKFS and the HO GKFS. When achieving comparable results, the numbers of control volumes (CV) of the 2O GKFS and the HO GKFS, are respectively 10 000 and 3600 for the quadrilateral mesh and 9902 and 2694 for the triangular mesh.

which consist of a primary vortex at the center of the cavity and two secondary vortices at the bottom left and bottom right corners of the cavity.

First, the effect of the virtual time step size on the accuracy of the high-order GKFS is investigated on the uniform quadrilateral mesh with 6400 cells. Three CFL numbers for calculation of  $\Delta t_p$  is tested, i.e.,  $\sigma_p = 0.5, 0.7,$  and  $0.9$ . It can be seen from Fig. 7 that the velocity profiles along the vertical and horizontal central lines agree well with the benchmark data<sup>63</sup> and are barely affected by the virtual time step size. Second, the accuracy of the high-order GKFS is compared with the second-order GKFS on the same mesh. As shown in Fig. 8, the high-order GKFS can obtain more accurate results than the second-order scheme on a uniform quadrilateral mesh with 3600 cells. Figures 9 and 10 depict the mesh convergence studies of the second-order GKFS and the high-order GKFS on the non-uniform triangular meshes, respectively. It is found that the high-order GKFS can achieve the comparable results of the

benchmark data<sup>63</sup> on a triangular mesh with 2694 control volumes, while the second-order GKFS requires a refined mesh with 9902 control volumes. In Fig. 11, we compare the convergence histories of the second-order GKFS and the high-order GKFS. Apparently, the high-order GKFS converges faster than the second-order counterpart when achieving comparable results. Furthermore, the

TABLE I. Comparison of the computational mesh and CPU time (seconds) of the 2O GKFS and the HO GKFS for lid-driven cavity flow when achieving comparable results.

Mesh	Scheme	Control volumes	CPU time	Speed-up ratio
Quadrilateral	2O GKFS	10 000	205.093	...
	HO GKFS	3600	95.250	2.153
Triangular	2O GKFS	9902	224.046	...
	HO GKFS	2694	62.312	3.596

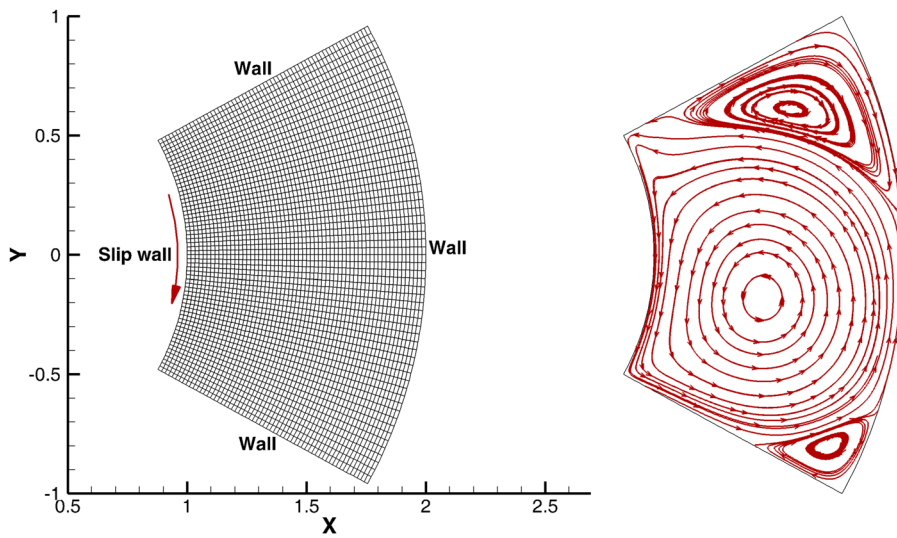


FIG. 12. Computational mesh for polar cavity flow (left) and streamlines calculated by the HO GKFS (right).

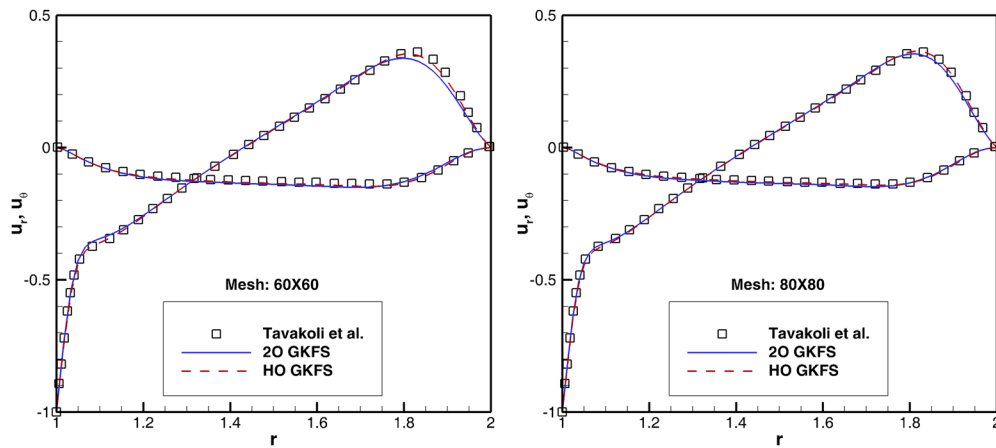


FIG. 13. Comparison of radial and azimuthal velocity distributions for polar cavity flow at  $\theta = 0$  on the uniform quadrilateral mesh with  $60 \times 60$  cells (left) and  $80 \times 80$  cells (right).

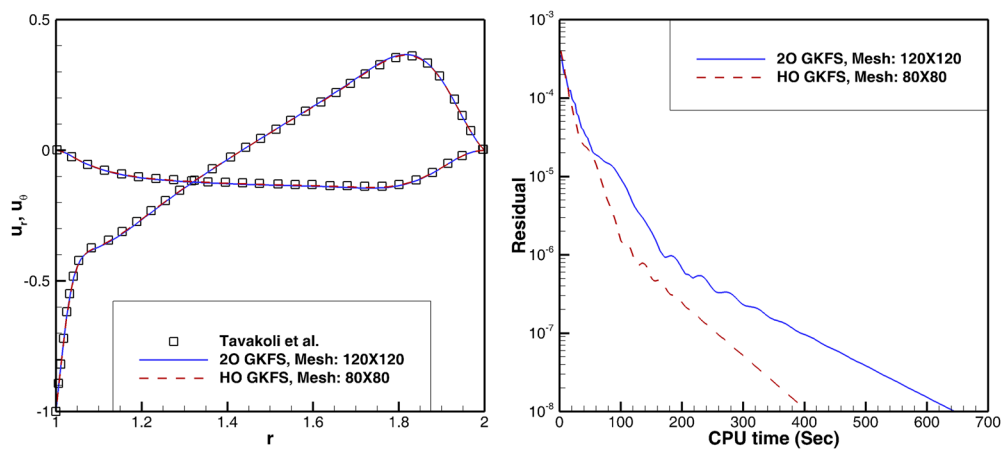
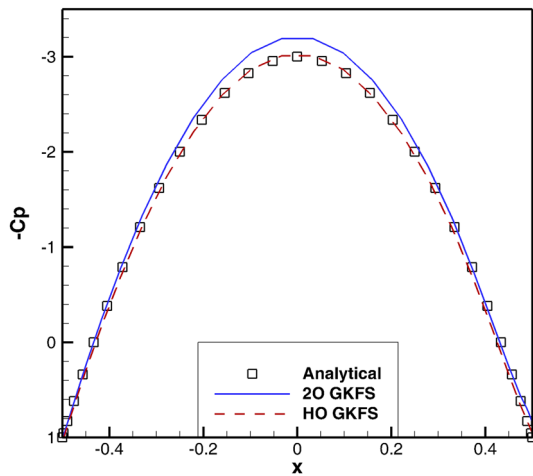


FIG. 14. Comparison of radial and azimuthal velocity distributions for polar cavity flow at  $\theta = 0$  (left) and the CPU time of the 2O GKFS and the HO GKFS (right) when achieving comparable results.



**FIG. 15.** Comparison of pressure coefficient distribution along the cylindrical surface calculated by the 2O GKFS and the HO GKFS.

computational mesh and the central processing unit (CPU) time of these two solvers are tabulated in Table I. The speed-up ratio of 3.596 can be achieved for the high-order GKFS on the triangular mesh when achieving comparable results.

**C. Case 3: Polar cavity flow**

In this section, the accuracy and efficiency of the high-order GKFS on the curved boundary are validated by the polar cavity flow.<sup>64</sup> As shown in Fig. 12, the computational domain of this test example is a sector with the angle of one radian and symmetric with respect to the *x*-axis. The radius of the inner arc and the outer arc is  $R_i = 1$  and  $R_o = 2$ , respectively. The inner arc is moving with the azimuthal velocity  $u_0$  and the other boundaries are fixed. The Reynolds number is defined as  $Re = \rho_0 u_0 (R_o - R_i) / \mu$  and set as 1000 in the present simulation. The computational domain is discretized by the uniform quadrilateral mesh with different sizes.

The streamlines obtained by the high-order GKFS on a mesh with  $60 \times 60$  cells are shown in Fig. 12, which are in line with the result of Tavakoli *et al.*<sup>64</sup> In Fig. 13, the simulation results of the second-order GKFS and the high-order GKFS are compared. It can be found that the results of the high-order GKFS are closer to the benchmark data<sup>64</sup> than the second-order one on the same grid and the high-order GKFS can provide accurate results on a mesh with  $80 \times 80$  cells. As displayed in Fig. 14, a fine mesh with  $120 \times 120$  cells is required for the second-order GKFS to achieve such results. Accordingly, the high-order GKFS requires less CPU time to obtain comparable results than the second-order counterpart. As shown in Fig. 14, the CPU time of these two solvers is about 400 s and 640 s, respectively.

**D. Case 4: Flow around a circular cylinder**

To validate the performance of the high-order GKFS for simulation of external flows, the flow around a circular cylinder is tested in this section. First, the inviscid flow around a circular cylinder is solved on an O-type grid with  $48 \times 48$  quadrilateral cells. The far-field boundary is taken  $30D$  away from the geometrical center of the cylinder, where  $D$  is the diameter of the cylinder, and the height of the cell adjacent to the wall is set as  $0.03D$ . The pressure coefficient distribution along the cylindrical surface is depicted in Fig. 15. As compared with the second-order GKFS, the result of the high-order GKFS is closer to the analytical data. The pressure contours obtained by these two solvers are shown in Fig. 16. It can be found that the symmetry of the solutions is well captured by the high-order GKFS.

Second, the viscous flow around a circular cylinder is simulated. In this test case, the flow pattern is governed by the Reynolds number  $Re = \rho_0 u_0 D / \mu$ , where  $\rho_0$  and  $u_0$  are the free stream density and velocity, respectively. In the simulation,  $Re = 20$  and  $40$  are considered. The same computational domain of the inviscid case is used but discretized by an O-type grid with  $120 \times 100$  quadrilateral cells. The height of the cell adjacent to the wall is set as  $0.01D$ . The pressure coefficient distribution around the cylindrical surface at  $Re = 40$  is depicted in Fig. 17 and compared with the results of He and Doolen.<sup>65</sup> Good agreement is observed and the results of

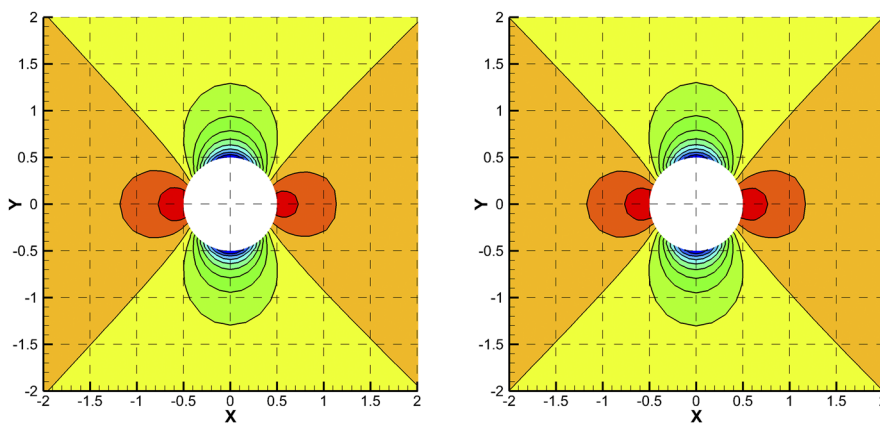


**FIG. 16.** Pressure contours calculated by the 2O GKFS (left) and the HO GKFS (right).

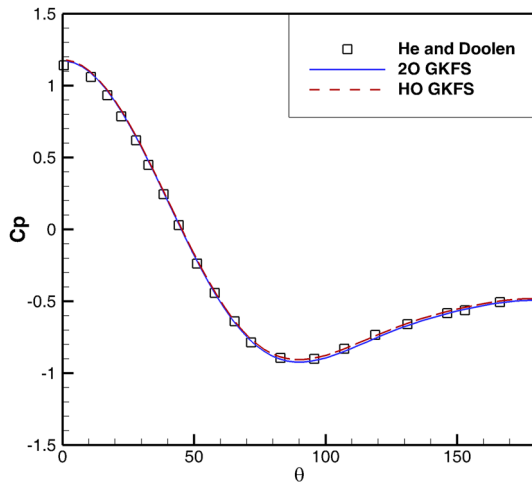


FIG. 17. Comparison of pressure coefficient distribution along the cylindrical surface at  $Re = 40$  calculated by the 2O GKFS and the HO GKFS.

the high-order GKFS are slightly better than the second-order one. The comparison of the drag coefficient, the recirculation length, and the separation angle with reference data<sup>66–68</sup> is made in Table II. In this table, the results calculated by the high-order GKFS with a fine mesh ( $240 \times 200$  quadrilateral cells) are taken as the benchmark data. It is found that the results of the high-order GKFS with  $120 \times 100$  quadrilateral cells are closer to the benchmark data than those of the second-order scheme, especially for the recirculation length.

**E. Case 5: Flow around a NACA0012 airfoil**

The last test case is the flow around a NACA0012 airfoil. In the simulation, the chord length-based Reynolds number is taken as 500 and the angle of attack is set as  $0^\circ$ . Two meshes are used to validate the superiority of the high-order GKFS. As shown in Fig. 18, the coarse mesh has 120 points on the airfoil surface and

TABLE II. Comparison of the drag coefficient, recirculation length, and separation angle for the flow around a circular cylinder at  $Re = 20$  and 40.

$Re$	References	$C_d$	$L_s/D$	$\theta_s$
20	Dennis and Chang <sup>66</sup>	2.05	0.94	43.7
	Shu <i>et al.</i> <sup>67</sup>	2.062	0.935	42.94
	Yang <i>et al.</i> <sup>68</sup>	2.059	0.921	43.73
	2O GKFS	2.065	0.896	43.38
	HO GKFS	2.051	0.922	43.51
	HO GKFS (fine mesh)	2.053	0.934	43.69
40	Dennis and Chang <sup>66</sup>	1.52	2.35	53.8
	Shu <i>et al.</i> <sup>67</sup>	1.530	2.240	52.69
	Yang <i>et al.</i> <sup>68</sup>	1.540	2.229	53.71
	2O GKFS	1.550	2.092	53.46
	HO GKFS	1.537	2.221	53.72
	HO GKFS (fine mesh)	1.537	2.294	53.80

6664 triangular cells, and the fine mesh has 200 points on the airfoil surface and 20 674 triangular cells. The far-field boundary is taken 20 times of chord length away from the airfoil. The pressure contours and  $u$ -velocity contours of this test case are shown in Fig. 19, where the symmetric distribution of the flow field about the  $x$ -axis is observed due to the zero angle of attack.

The pressure coefficient and skin friction coefficient distributions along the airfoil surface are depicted in Fig. 20. Also displayed in this figure are the results of Hafez *et al.*<sup>69</sup> and Khorasanizade and Sousa.<sup>70</sup> It can be found that the results of the second-order GKFS with the coarse mesh have some oscillations, which can be suppressed by using the fine mesh. In contrast, for the high-order GKFS, the results of the coarse mesh match well with those of the second-order GKFS with the fine mesh and the reference data.<sup>69,70</sup> This test case shows that the high-order GKFS can provide more accurate results than the second-order counterpart on a relatively coarse mesh.

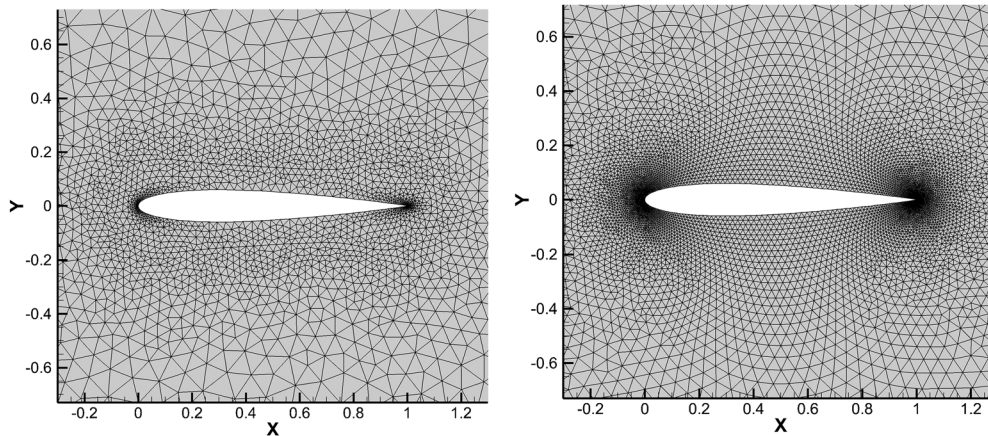


FIG. 18. Computational mesh for flow around a NACA0012 airfoil: left: coarse mesh; right: fine mesh.

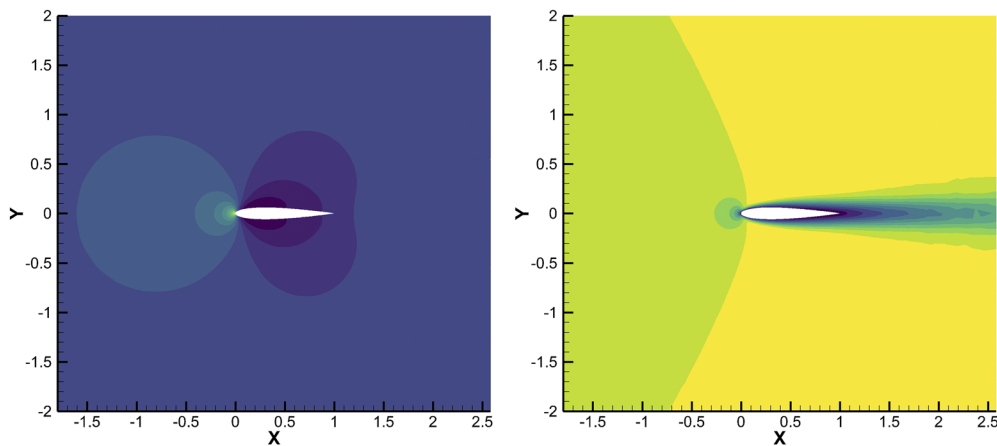


FIG. 19. Pressure contours (left) and  $u$ -velocity contours (right) for flow around a NACA0012 airfoil calculated by the HO GKFS on a fine mesh.

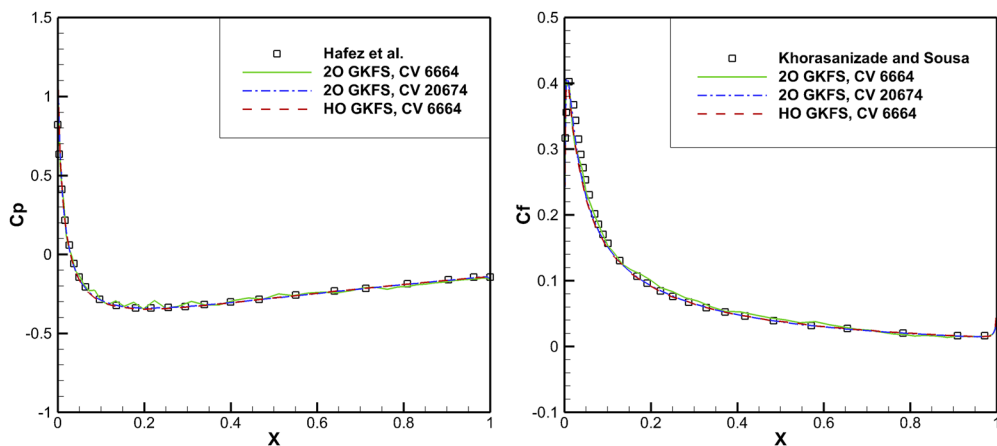


FIG. 20. Comparison of pressure coefficient distribution (left) and skin friction coefficient distribution (right) for flow around a NACA0012 airfoil.

## V. CONCLUSIONS

This work presents a high-order GKFS for simulation of incompressible flows on the unstructured mesh. In this method, the local asymptotic solution to the Boltzmann equation with high-order accuracy is used to calculate the inviscid and viscous fluxes of the Navier–Stokes equations simultaneously. This local asymptotic solution has the second-order accuracy in time and the fourth-order accuracy in space. Since the time step size of the solution reconstruction is independent of the time step size of solving the Navier–Stokes equations, the temporal accuracy of the numerical flux may not affect the overall accuracy of the high-order GKFS. As compared with the high-order GKS,<sup>49–53</sup> the developed high-order GKFS is a bit simple and the expression of the numerical flux of the Navier–Stokes equations can be given concisely.

Five test cases including the decaying vortex flow, the lid-driven cavity flow, the polar cavity flow, the flow around a circular cylinder, and the flow around a NACA0012 airfoil are simulated to validate

the accuracy and efficiency of the high-order GKFS on the quadrilateral mesh and the triangular mesh. It is shown that the high-order GKFS can achieve the desired accuracy on both meshes. At the same time, the accuracy of the high-order GKFS is not affected by the virtual time step size used in the solution reconstruction, while for the high-order FV scheme of Liu *et al.*,<sup>32</sup> the order of accuracy degrades as the virtual time step size is increased to violate the requirement of interpolation for the solution reconstruction. As compared with the second-order GKFS, the high-order scheme can provide comparable results with less computational time.

Since the weakly compressible Navier–Stokes equations under the low Mach number limit are used in this work, the present method can only be used to simulate isothermal incompressible flows. To extend its application to compressible flows as well as non-isothermal flows, the energy equation should be involved and the equilibrium distribution function should be changed accordingly. Like the high-order GKFS for isothermal incompressible flows, the formulation of the high-order GKFS for compressible flows can



also be given explicitly, but it is a little bit more complicated than the incompressible one. The details of the high-order GKFS for compressible flows will be presented in future work.

## ACKNOWLEDGMENTS

The research was partially supported by the National Natural Science Foundation of China (Grant Nos. 11772157 and 11832012), the National Numerical Wind Tunnel Project of China (Grant No. NNW2019ZT2-B28), and the Priority Academic Program Development of Jiangsu Higher Education Institutions (PAPD).

## DATA AVAILABILITY

The data that support the findings of this study are available within the article.

## REFERENCES

- <sup>1</sup>S. Laizet, E. Lamballais, and J. C. Vassilicos, "A numerical strategy to combine high-order schemes, complex geometry and parallel computing for high resolution DNS of fractal generated turbulence," *Comput. Fluids* **39**(3), 471–484 (2010).
- <sup>2</sup>R. Yu, J. Yu, and X.-S. Bai, "An improved high-order scheme for DNS of low Mach number turbulent reacting flows based on stiff chemistry solver," *J. Comput. Phys.* **231**(16), 5504–5521 (2012).
- <sup>3</sup>Y. Kaneda, T. Ishihara, M. Yokokawa, K. I. Itakura, and A. Uno, "Energy dissipation rate and energy spectrum in high resolution direct numerical simulations of turbulence in a periodic box," *Phys. Fluids* **15**(2), L21–L24 (2003).
- <sup>4</sup>C. Mao, T. Jin, K. Luo, and J. Fan, "Investigation of supersonic turbulent flows over a sphere by fully resolved direct numerical simulation," *Phys. Fluids* **31**(5), 056102 (2019).
- <sup>5</sup>S. Nagarajan, S. K. Lele, and J. H. Ferziger, "A robust high-order compact method for large eddy simulation," *J. Comput. Phys.* **191**(2), 392–419 (2003).
- <sup>6</sup>D. P. Rizzetta, M. R. Visbal, and G. A. Blaisdell, "A time-implicit high-order compact differencing and filtering scheme for large-eddy simulation," *Int. J. Numer. Methods Fluids* **42**(6), 665–693 (2003).
- <sup>7</sup>M. Minguez, R. Pasquetti, and E. Serre, "High-order large-eddy simulation of flow over the 'Ahmed body' car model," *Phys. Fluids* **20**(9), 095101 (2008).
- <sup>8</sup>D. Oberle, C. D. Pruett, and P. Jenny, "Temporal large-eddy simulation based on direct deconvolution," *Phys. Fluids* **32**(6), 065112 (2020).
- <sup>9</sup>M. Zhuang and R. F. Chen, "Applications of high-order optimized upwind schemes for computational aeroacoustics," *AIAA J.* **40**(3), 443–449 (2002).
- <sup>10</sup>S. Marié, D. Ricot, and P. Sagaut, "Comparison between lattice Boltzmann method and Navier–Stokes high order schemes for computational aeroacoustics," *J. Comput. Phys.* **228**(4), 1056–1070 (2009).
- <sup>11</sup>A. Langenais, F. Vuillot, J. Troyes, and C. Bailly, "Accurate simulation of the noise generated by a hot supersonic jet including turbulence tripping and nonlinear acoustic propagation," *Phys. Fluids* **31**(1), 016105 (2019).
- <sup>12</sup>A. Nejat and C. Ollivier-Gooch, "A high-order accurate unstructured finite volume Newton–Krylov algorithm for inviscid compressible flows," *J. Comput. Phys.* **227**(4), 2582–2609 (2008).
- <sup>13</sup>S. Clain, S. Diot, and R. Loubère, "A high-order finite volume method for systems of conservation laws—Multi-dimensional optimal order detection (MOOD)," *J. Comput. Phys.* **230**(10), 4028–4050 (2011).
- <sup>14</sup>Q. Wang, Y.-X. Ren, J. Pan, and W. Li, "Compact high order finite volume method on unstructured grids III: Variational reconstruction," *J. Comput. Phys.* **337**, 1–26 (2017).
- <sup>15</sup>*Discontinuous Galerkin Methods: Theory, Computation and Applications*, edited by B. Cockburn, G. E. Karniadakis, and C. W. Shu (Springer Science & Business Media, 2012), Vol. 11.
- <sup>16</sup>T. Chen and C.-W. Shu, "Entropy stable high order discontinuous Galerkin methods with suitable quadrature rules for hyperbolic conservation laws," *J. Comput. Phys.* **345**, 427–461 (2017).
- <sup>17</sup>Z. Sun, J. Liu, and P. Wang, "A discontinuous Galerkin method by patch reconstruction for convection-diffusion problems," *Adv. Appl. Math. Mech.* **12**(3), 729–747 (2020).
- <sup>18</sup>H. T. Huynh, Z. J. Wang, and P. E. Vincent, "High-order methods for computational fluid dynamics: A brief review of compact differential formulations on unstructured grids," *Comput. Fluids* **98**, 209–220 (2014).
- <sup>19</sup>H. Ranocha, P. Öffner, and T. Sonar, "Summation-by-parts operators for correction procedure via reconstruction," *J. Comput. Phys.* **311**, 299–328 (2016).
- <sup>20</sup>Z. J. Wang and Y. Liu, "Extension of the spectral volume method to high-order boundary representation," *J. Comput. Phys.* **211**(1), 154–178 (2006).
- <sup>21</sup>Y. Sun, Z. J. Wang and Y. Liu, "High-order multidomain spectral difference method for the Navier–Stokes equations," in *44th AIAA Aerospace Sciences Meeting and Exhibit* (American Institute of Aeronautics and Astronautics, 2006), p. 301.
- <sup>22</sup>C. W. Shu, "Essentially non-oscillatory and weighted essentially non-oscillatory schemes for hyperbolic conservation laws," in *Advanced Numerical Approximation of Nonlinear Hyperbolic Equations* (Springer, Berlin, Heidelberg, 1998), pp. 325–432.
- <sup>23</sup>R. Borges, M. Carmona, B. Costa, and W. S. Don, "An improved weighted essentially non-oscillatory scheme for hyperbolic conservation laws," *J. Comput. Phys.* **227**(6), 3191–3211 (2008).
- <sup>24</sup>Y. Ha, C. Ho Kim, Y. Ju Lee, and J. Yoon, "An improved weighted essentially non-oscillatory scheme with a new smoothness indicator," *J. Comput. Phys.* **232**(1), 68–86 (2013).
- <sup>25</sup>Y. Wang, J. Zhu, and L. Xiong, "A new fifth-order trigonometric WENO scheme for hyperbolic conservation laws and highly oscillatory problems," *Adv. Appl. Math. Mech.* **11**(5), 1114–1135 (2019).
- <sup>26</sup>W. Li and Y.-X. Ren, "High-order  $k$ -exact WENO finite volume schemes for solving gas dynamic Euler equations on unstructured grids," *Int. J. Numer. Methods Fluids* **70**(6), 742–763 (2012).
- <sup>27</sup>L. Cueto-Felgueroso, I. Colominas, X. Nogueira, F. Navarrina, and M. Casteleiro, "Finite volume solvers and moving least-squares approximations for the compressible Navier–Stokes equations on unstructured grids," *Comput. Methods Appl. Mech. Eng.* **196**(45–48), 4712–4736 (2007).
- <sup>28</sup>Q. Wang, Y.-X. Ren, and W. Li, "Compact high order finite volume method on unstructured grids II: Extension to two-dimensional Euler equations," *J. Comput. Phys.* **314**, 883–908 (2016).
- <sup>29</sup>Y. Liu, W. Zhang, Y. Jiang, and Z. Ye, "A high-order finite volume method on unstructured grids using RBF reconstruction," *Comput. Math. Appl.* **72**(4), 1096–1117 (2016).
- <sup>30</sup>T. Barth and P. Frederickson, "Higher order solution of the Euler equations on unstructured grids using quadratic reconstruction," in *28th Aerospace Sciences Meeting* (American Institute of Aeronautics and Astronautics, 1990), p. 13.
- <sup>31</sup>T. Barth, "Recent developments in high order  $k$ -exact reconstruction on unstructured meshes," in *31st Aerospace Sciences Meeting* (American Institute of Aeronautics and Astronautics, 1993), p. 668.
- <sup>32</sup>Y. Y. Liu, C. Shu, H. W. Zhang, and L. M. Yang, "A high order least square-based finite difference-finite volume method with lattice Boltzmann flux solver for simulation of incompressible flows on unstructured grids," *J. Comput. Phys.* **401**, 109019 (2020).
- <sup>33</sup>Y. Y. Liu, H. W. Zhang, L. M. Yang, and C. Shu, "High-order least-square-based finite-difference-finite-volume method for simulation of incompressible thermal flows on arbitrary grids," *Phys. Rev. E* **100**(6), 063308 (2019).
- <sup>34</sup>F. Bassi and S. Rebay, "A high-order accurate discontinuous finite element method for the numerical solution of the compressible Navier–Stokes equations," *J. Comput. Phys.* **131**(2), 267–279 (1997).
- <sup>35</sup>K. J. Fidkowski, T. A. Oliver, J. Lu, and D. L. Darmofal, " $p$ -Multigrid solution of high-order discontinuous Galerkin discretizations of the compressible Navier–Stokes equations," *J. Comput. Phys.* **207**(1), 92–113 (2005).
- <sup>36</sup>Z. J. Wang, "High-order methods for the Euler and Navier–Stokes equations on unstructured grids," *Prog. Aerosp. Sci.* **43**(1–3), 1–41 (2007).
- <sup>37</sup>K. Xu, "A gas-kinetic BGK scheme for the Navier–Stokes equations and its connection with artificial dissipation and Godunov method," *J. Comput. Phys.* **171**(1), 289–335 (2001).

- <sup>38</sup>K. Xu and X. He, "Lattice Boltzmann method and gas-kinetic BGK scheme in the low-Mach number viscous flow simulations," *J. Comput. Phys.* **190**(1), 100–117 (2003).
- <sup>39</sup>J. Li, C. Zhong, Y. Wang, and C. Zhuo, "Implementation of dual time-stepping strategy of the gas-kinetic scheme for unsteady flow simulations," *Phys. Rev. E* **95**(5), 053307 (2017).
- <sup>40</sup>D. Zhou, Z. Lu, T. Guo, and G. Chen, "A loosely-coupled gas-kinetic BGK scheme for conjugate heat transfer in hypersonic flows," *Int. J. Heat Mass Transfer* **147**, 119016 (2020).
- <sup>41</sup>Y. Sun, C. Shu, C. J. Teo, Y. Wang, and L. M. Yang, "Explicit formulations of gas-kinetic flux solver for simulation of incompressible and compressible viscous flows," *J. Comput. Phys.* **300**, 492–519 (2015).
- <sup>42</sup>L. M. Yang, C. Shu, and J. Wu, "A simple distribution function-based gas-kinetic scheme for simulation of viscous incompressible and compressible flows," *J. Comput. Phys.* **274**, 611–632 (2014).
- <sup>43</sup>L. M. Yang, C. Shu, and Y. Wang, "Development of a discrete gas-kinetic scheme for simulation of two-dimensional viscous incompressible and compressible flows," *Phys. Rev. E* **93**(3), 033311 (2016).
- <sup>44</sup>Q. Huang, D. Zhang, and G. Pan, "Computational model construction and analysis of the hydrodynamics of a *Rhinoptera javanica*," *IEEE Access* **8**, 30410–30420 (2020).
- <sup>45</sup>Y. Li, X. D. Niu, A. Khan, D. C. Li, and H. Yamaguchi, "A numerical investigation of dynamics of bubbly flow in a ferrofluid by a self-correcting procedure-based lattice Boltzmann flux solver," *Phys. Fluids* **31**(8), 082107 (2019).
- <sup>46</sup>Y. Wang, C. Shu, C. J. Teo, and L. M. Yang, "Numerical study on the freely falling plate: Effects of density ratio and thickness-to-length ratio," *Phys. Fluids* **28**(10), 103603 (2016).
- <sup>47</sup>Y. Wang, C. Shu, and L. M. Yang, "An improved multiphase lattice Boltzmann flux solver for three-dimensional flows with large density ratio and high Reynolds number," *J. Comput. Phys.* **302**, 41–58 (2015).
- <sup>48</sup>B. Walsh and F. J. Boyle, "A preconditioned lattice Boltzmann Flux solver for steady flows on unstructured hexahedral grids," *Comput. Fluids* **210**, 104634 (2020).
- <sup>49</sup>Q. Li, K. Xu, and S. Fu, "A high-order gas-kinetic Navier–Stokes flow solver," *J. Comput. Phys.* **229**(19), 6715–6731 (2010).
- <sup>50</sup>X. Ren, K. Xu, W. Shyy, and C. Gu, "A multi-dimensional high-order discontinuous Galerkin method based on gas kinetic theory for viscous flow computations," *J. Comput. Phys.* **292**, 176–193 (2015).
- <sup>51</sup>L. Pan and K. Xu, "A third-order gas-kinetic scheme for three-dimensional inviscid and viscous flow computations," *Comput. Fluids* **119**, 250–260 (2015).
- <sup>52</sup>X. Ji, L. Pan, W. Shyy, and K. Xu, "A compact fourth-order gas-kinetic scheme for the Euler and Navier–Stokes equations," *J. Comput. Phys.* **372**, 446–472 (2018).
- <sup>53</sup>X. Ji, F. Zhao, W. Shyy, and K. Xu, "A family of high-order gas-kinetic schemes and its comparison with Riemann solver based high-order methods," *J. Comput. Phys.* **356**, 150–173 (2018).
- <sup>54</sup>Y. Sun, L. Yang, C. Shu, and Y. Chen, "A diffuse-interface immersed boundary method for simulation of compressible viscous flows with stationary and moving boundaries," *Int. J. Numer. Methods Fluids* **92**(3), 149–168 (2020).
- <sup>55</sup>C.-W. Shu and S. Osher, "Efficient implementation of essentially non-oscillatory shock-capturing schemes," *J. Comput. Phys.* **77**(2), 439–471 (1988).
- <sup>56</sup>S. Yoon and A. Jameson, "Lower-upper symmetric-Gauss-Seidel method for the Euler and Navier-Stokes equations," *AIAA J.* **26**(9), 1025–1026 (1988).
- <sup>57</sup>H. Ding, C. Shu, K. S. Yeo, and D. Xu, "Development of least-square-based two-dimensional finite-difference schemes and their application to simulate natural convection in a cavity," *Comput. Fluids* **33**(1), 137–154 (2004).
- <sup>58</sup>S. Chen and G. D. Doolen, "Lattice Boltzmann method for fluid flows," *Annu. Rev. Fluid Mech.* **30**(1), 329–364 (1998).
- <sup>59</sup>H. Lai and C. Ma, "Lattice Boltzmann method for the generalized Kuramoto–Sivashinsky equation," *Physica A* **388**(8), 1405–1412 (2009).
- <sup>60</sup>K. Wang, L. Yang, Y. Yu, and G. Hou, "Influence of slip boundary on the hydrofoil with a curved slip boundary condition for the lattice Boltzmann method," *Phys. Fluids* **30**(12), 123601 (2018).
- <sup>61</sup>*Lattice Boltzmann and Gas Kinetic Flux Solvers: Theory and Applications*, edited by L. M. Yang, Y. Wang, Z. Chen, and C. Shu (World Scientific, 2020), Vol. 1.
- <sup>62</sup>J. Blazek, *Computational Fluid Dynamics: Principles and Applications* (Butterworth-Heinemann, 2015).
- <sup>63</sup>U. Ghia, K. N. Ghia, and C. T. Shin, "High-Re solutions for incompressible flow using the Navier–Stokes equations and a multigrid method," *J. Comput. Phys.* **48**(3), 387–411 (1982).
- <sup>64</sup>E. Tavakoli, B. Lessani, and R. Hosseini, "High-order pole-treatment in cylindrical coordinates for incompressible flow simulations with finite-difference collocated schemes," *J. Comput. Phys.* **296**, 1–24 (2015).
- <sup>65</sup>X. He and G. Doolen, "Lattice Boltzmann method on curvilinear coordinates system: Flow around a circular cylinder," *J. Comput. Phys.* **134**(2), 306–315 (1997).
- <sup>66</sup>S. C. R. Dennis and G.-Z. Chang, "Numerical solutions for steady flow past a circular cylinder at Reynolds numbers up to 100," *J. Fluid Mech.* **42**(3), 471–489 (1970).
- <sup>67</sup>C. Shu, Y. Wang, C. J. Teo, and J. Wu, "Development of lattice Boltzmann flux solver for simulation of incompressible flows," *Adv. Appl. Math. Mech.* **6**(4), 436–460 (2014).
- <sup>68</sup>L. M. Yang, C. Shu, W. M. Yang, and Y. Wang, "A simplified circular function-based gas kinetic scheme for simulation of incompressible flows," *Int. J. Numer. Methods Fluids* **85**(10), 583–598 (2017).
- <sup>69</sup>M. Hafez, A. Shatalov, and E. Wahba, "Numerical simulations of incompressible aerodynamic flows using viscous/inviscid interaction procedures," *Comput. Methods Appl. Mech. Eng.* **195**(23–24), 3110–3127 (2006).
- <sup>70</sup>S. Khorasanizade and J. M. M. Sousa, "An adaptive fully-Lagrangian meshless method for incompressible laminar flow airfoil studies," *Aerosp. Sci. Technol.* **64**, 161–170 (2017).